



Department of Physics

Final Year Project

**Optical Studies of Distributed Feedback
Resonators with Perovskite
Nanocrystal Gain Media**

Elena Kyprianou

Supervisor: Dr. Grigorios Itskos

A Final Year Project submitted to the University of Cyprus in partial fulfilment of the requirements for the undergraduate degree in Physics.

May 2021

“Remember to look up at the stars and not down at your feet. Try to make sense of what you see and wonder about what makes the universe exist. Be curious. And however difficult life may seem, there is always something you can do and succeed at. It matters that you don't just give up.”

Stephen Hawking

Acknowledgments

Foremost, I would like to express my deepest gratitude to my supervisor, Associate Professor Grigorios Itskos for the opportunity and the trust to work with his group and perform my thesis under his guidance. His continuous support, encouragement, and helpful advice throughout the duration of this project were invaluable for the completion of this project. I appreciate all his suggestions and feedback both on experimental work and writing of this thesis. His extensive knowledge, and enthusiasm for his work were inspiring and motivational for me. It was a great honour and pleasure to work under his guidance.

I would like to extend my sincere appreciation to postdoctoral researcher, Dr. Modestos Athanasiou for his valuable support and patient guidance. He helped me to learn the methodology of performing an experiment and analyse and present the results clearly and precisely. Without his help this project would not have been completed.

Special thanks also to Andreas Manoli and Paris Papagiorgis for their help in the laboratory.

Abstract and Motivation

Colloidal semiconductor nanocrystals (NCs) have recently emerged as promising materials for various applications due to their extraordinary optical properties combined with facile solution-based colloidal synthesis. The typical diameter of colloidal nanocrystals (CNCs) is 2-20 nm, resulting in quantum-size effects, such as quantum confinement. A result of the quantum confinement in semiconductor NCs, is the strong dependence of electronic structure on NC size, enabling the tailoring of their bandgap by varying their size. A new class of CNCs is lead halide perovskite (LHP) NCs, used in this project. LHP NCs exhibit outstanding optical properties rendering them promising candidates for optoelectronic applications, such as light-emitting diodes, lasers and displays. Their optical properties include high photoluminescence quantum yields (PL QYs), approaching unity, tunability of their emission spectra over the entire visible spectral range arising from their versatile surface chemistry that enables tuning of their chemical composition, and narrow emission line widths leading to highly saturated colours.

In this project, the optical properties of distributed feedback (DFB) resonators with cesium lead bromide (CsPbBr_3) perovskite NCs as the gain medium, were studied. The motivation to use DFB gratings emerges from their potential to achieve narrow single mode emission, with line widths less than 1nm and low lasing thresholds, and also their potential for integration with other devices. These features of DFB resonators render them more suitable candidates for lasing applications, compared with other types of resonators, such as Fabry-Perot and whispering gallery mode. As the active material of the DFB resonators, fully inorganic CsPbBr_3 NCs were selected due to their improved thermal and structural stability and higher PL QYs, with respect to hybrid organic-inorganic perovskite NCs. For the optical characterization of the DFB-NC structures, steady state, time-resolved, and angle-resolved PL experiments were performed. Furthermore, angle-resolved transmission of the nanostructures was investigated revealing the photonic band dispersion of the probed structures. The reported results include strong modification of the lineshape, intensity, and polarization of NC PL, arising from coupling with the TM DFB cavity mode for a DFB grating with period $\Lambda=278$ nm. The NC PL characteristics were also investigated for a DFB grating with $\Lambda=416$ nm. In addition, optical modelling was performed to predict the properties of the nanostructures under investigation.

Table of Contents:

Acknowledgments.....	1
Abstract and Motivation	2
1. Theoretical Background	4
1.1 Introduction to Colloidal Nanocrystals	4
1.2 Lead Halide Perovskite Nanocrystals	5
1.2.1 Crystal structure.....	5
1.2.2 Optoelectronic properties.....	6
1.2.3 Defect-tolerance	7
1.2.4 Structural and Thermal lability.....	8
1.3 Stimulated Emission.....	10
1.3.1 Fundamental processes of light-matter interaction	10
1.3.2 Amplified Spontaneous Emission (ASE)	11
1.4 Introduction to optical resonators.....	12
1.4.1 Distributed Feedback Bragg (DFB) resonators.....	13
2. Experimental Methods.....	17
2.1 Film Deposition	17
2.2 Optical Modelling.....	18
2.3 Spectroscopic Techniques.....	20
2.3.1 Absorption Setup	20
2.3.2 Photoluminescence Setup	21
2.3.3 Optical microscope setup	25
2.3.4 Angle-resolved Photoluminescence and Transmission setup	27
3. Results and Discussion	28
3.1 Data Analysis.....	28
3.2 Optical characterization of DFB gratings with CsPbBr ₃ NC overlayers	29
3.2.1 Steady state photoluminescence measurements.....	31
3.2.2 Time-resolved photoluminescence measurements	35
3.2.3 Angle-resolved Photoluminescence and Transmission measurements	39
4. Conclusions and Future Work.....	46
5. References	48
Appendix	1
Optical modelling.....	1

1. Theoretical Background

1.1 Introduction to Colloidal Nanocrystals

Colloidal semiconductor nanocrystals (NCs) are nanocrystallites with sizes in the range of few to tens of nanometers. Nanocrystals are distinguished to weakly confined and strongly confined NCs, based on the degree of quantum confinement. In the weak confinement case, the exciton Bohr radius is smaller than the radius of the NC, resulting in quantization of the exciton center-of-mass motion. Strong confinement occurs when the exciton Bohr radius is larger than the NC's radius, and at this case the NCs are also referred to as quantum dots (QDs).^[1] These QDs exhibit strong quantum-size effects, which enhance their light absorption and emission properties with respect to their bulk counterparts. NCs and QDs can be synthesized with colloidal chemistry methods and their properties can be controlled by adding surface capping ligands (surfactants). Such surfactants can eliminate the mid-gap states that are formed due to surface dangling bonds, providing the proper surface passivation and enhancement of the NC emission. Simultaneously, the ligands control the nucleation, growth and long-term stability of semiconductor NCs. ^{[2]–[4]}

The synthesis of colloidal nanocrystal solutions can be achieved by reacting appropriate molecular precursors, such as inorganic salts or organometallic compounds. The process of colloidal synthesis comprises several stages (**Figure 1.1**). The first stage is the nucleation from an initially homogeneous solution. After the nucleation, the growth of the preformed nuclei takes place, followed by the isolation of the particles that have reached the desired size from the reaction mixture. ^[2]

For NCs with narrow size distribution a temporal separation of the nucleation stage from the growth of the nanoparticles is required. This requirement can be fulfilled by various methods, the most successful being the hot-injection method. In the hot-injection method, a solution of precursor molecules, at room temperature, is rapidly injected into a hot solvent, resulting to reduction of the temperature of the hot solvent. The rapid injection of cold precursor solution into the hot solvent leads to a rapid nucleation. However, the subsequent temperature drop prevents the further formation of new nuclei and thus the nucleation process is terminated. A gently reheating results in slow growth of the nanocrystals. The most common mechanism for the growth of NCs is the Ostwald ripening mechanism, where the small particles in the solution are dissolved easier than larger particles. The result is that material from the small particles is slowly diffused to the larger particles. ^{[5]–[7]}

The motivation for the study and use of NCs for a variety of applications emerges from their high absorption, high emission efficiency, narrow spectra, and facile and low-cost fabrication methods.

Furthermore, the bandgap of such NCs can be easily tuned by varying their size. The characteristics of colloidal semiconductor NCs mentioned, render them promising candidates for displays, light-emitting devices, bio-imaging and solar cells.

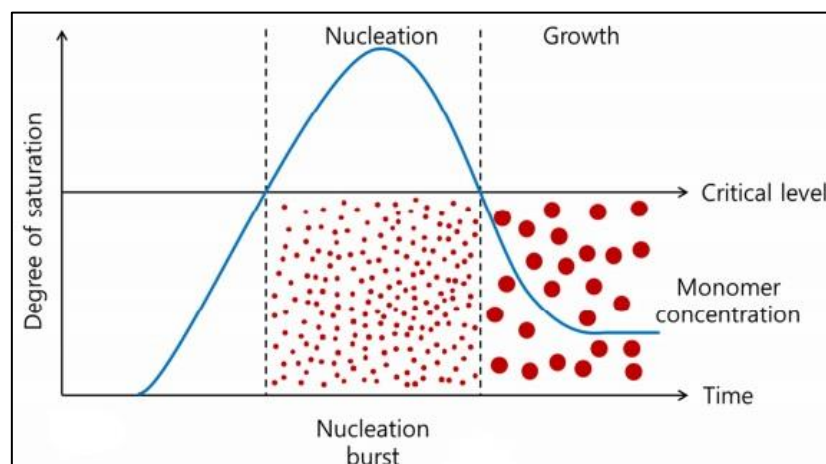


Figure 1.1: Stages of colloidal synthesis: nucleation and growth mechanisms. ^[7]

1.2 Lead Halide Perovskite Nanocrystals

Lead halide perovskite nanocrystals (LHP NCs) are colloidal nanocrystals that crystallize in a perovskite-type lattice. Fully inorganic LHP NCs (CsPbX_3 with $\text{X} = \text{Cl}^-$, Br^- or I^-) were produced in the 1950s and found to exhibit semiconductive properties. In the late 1970s, hybrid organic-inorganic LHPs, MAPbX_3 ($\text{MA} = \text{CH}_3\text{NH}_3^+$; methylammonium) and FAPbX_3 ($\text{FA} = \text{CH}(\text{NH}_2)_2^+$; formamidinium), were first reported. ^[8] In the form of robust, fully inorganic colloidal nanocrystals, they were first demonstrated in 2015 by the group of M. Kovalenko. ^[3]

The facile synthesis of such NCs, combined with their outstanding optical properties have rendered them promising candidates for optoelectronic applications and initiated a large research effort by the science community towards the understanding of their properties.

1.2.1 Crystal structure

LHPs crystallize in the APbX_3 -type perovskite lattice (where A is MA, FA or Cs^+ , and X is one or a combination of halides Cl^- , Br^- or I^-). The characteristic of this lattice type is the three-dimensional (3D) interconnection of the corner-sharing $[\text{PbX}_6]^{4-}$ octahedra, with the large voids in between occupied by the A-site cations (**Figure 1.2 a**). ^[9] The most common 3D polymorphs of perovskite lattice are the cubic, tetragonal and orthorhombic. The highest temperature (room temperature) phase is the cubic which is also the most symmetric and the most stable and suitable for applications. The

symmetry decreases for the tetragonal phase and even more for the orthorhombic, which is the least symmetric phase, and it occurs at low temperatures. In general, the phase transitions have well-defined temperatures, which are dependent by the anion/cation in the perovskite lattice and the surface ligands. [8]

The 3D polymorphs of the perovskite structure have the largest electronic delocalization, with respect to 2D and 1D polymorphs, resulting in the semiconducting properties of 3D LHPs. The lower dimensionality polymorphs (2D, 1D or 0D) exhibit larger bandgaps and thus they do not typically show semiconducting properties.

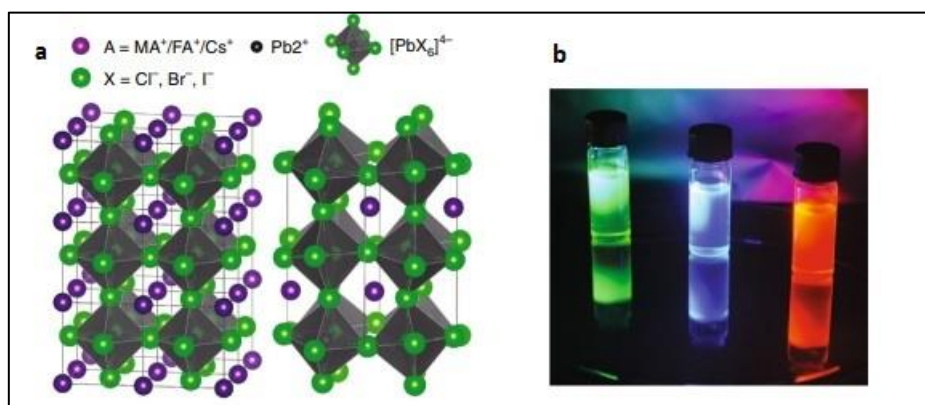


Figure 1.2: a. The $APbX_3$ -type perovskite lattice of LHPs with three-dimensional corner-sharing octahedra. On the left, the cubic structure is shown ($MAPbX_3$, $FAPbX_3$) and on the right the orthorhombic ($CsPbX_3$). b. Colloidal solutions of highly luminescent LHP NCs. Left: $CsPbBr_3$ with emission peak at 520 nm, middle: $CsPb(Cl/Br)_3$ with emission peak at 450 nm and right: $FAPb(Br/I)_3$ with emission peak at 640 nm. [9]

1.2.2 Optoelectronic properties

An important feature of LHP NCs is the tunability of their photoluminescence (PL) and absorption spectra over the entire visible spectral range both via tuning the size and shape, but mainly through compositional modulations, such as anion and cation exchange that occur easily due to the ionic nature of bonding in the perovskite crystal (**Figure 1.3**). The relationship between the electronic structure and particle size arises from the quantum confinement in NCs [2]. The high PL quantum yield (QY) is another advantageous attribute of LHP NCs and is associated with the defect-tolerance of LHP NCs (which is explained in detail in the section **1.2.3**). The PL of LHP NCs is characterized by narrow emission line widths leading to highly saturated colours. The high PL QYs and the highly saturated colours make LHP NCs suitable materials for optoelectronic applications such as liquid-crystal displays (LCDs) and light-emitting devices. [3],[8]

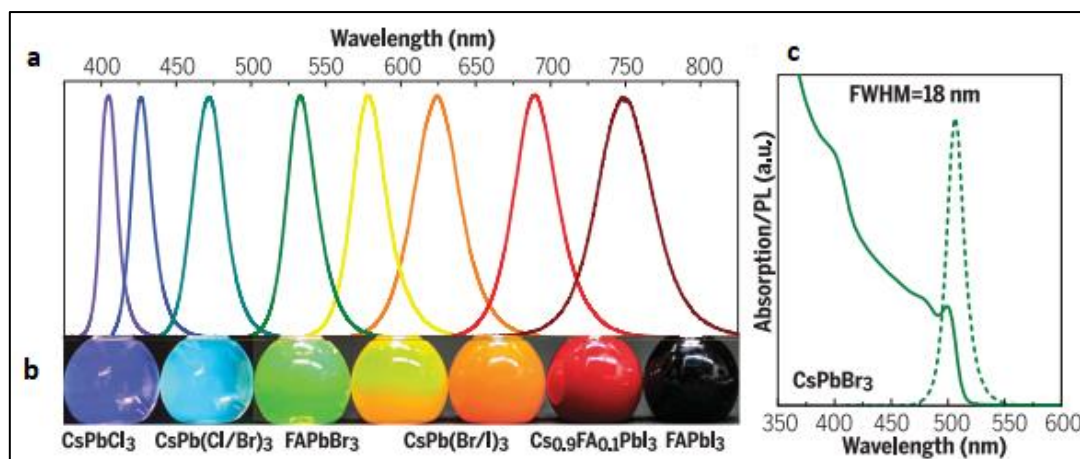


Figure 1.3: **a.** PL spectra covering the entire visible spectral region by tuning the composition and particle size and **b.** the corresponding photographs of composition-tuned LHP NCs under mixed daylight and UV excitation. **c.** PL (dash line) and absorption (solid line) spectra of 8-nm $CsPbBr_3$ NCs. ^[8]

1.2.3 Defect-tolerance

The major type of point defects formed in LHP NCs is vacancies due to their low formation energy. The vacancies, in LHP bulk and nanocrystal materials, are typically shallow defects which do not form mid-gap trap states. Other point defects such as interstitials and antisites, which can form deep trap states where the carriers can be efficiently trapped, are not typically formed in LHP NCs due to their high formation energies (**Figure 1.4 a**). The high PL QYs of LHP NCs emerge from such absence of deep traps, that are detrimental to the emission process, as well as from their defect-tolerant electronic structure. The bandgap in LHPs, is formed between two antibonding orbitals thus the vacancies form only shallow defects or states that are enclosed in the valence or conduction band (**Figure 1.4 b**). The result is that these vacancy-related states do not influence the radiative recombination and other optical properties of LHP NCs. In contrary, in defect-intolerant semiconductors the bandgap is formed between bonding and antibonding orbitals resulting in the formation of mid-gap trap states. The carriers can be trapped in the mid-gap states leading to reduction of radiative recombination rendering conventional semiconductor NCs poorly luminescent. ^[9]

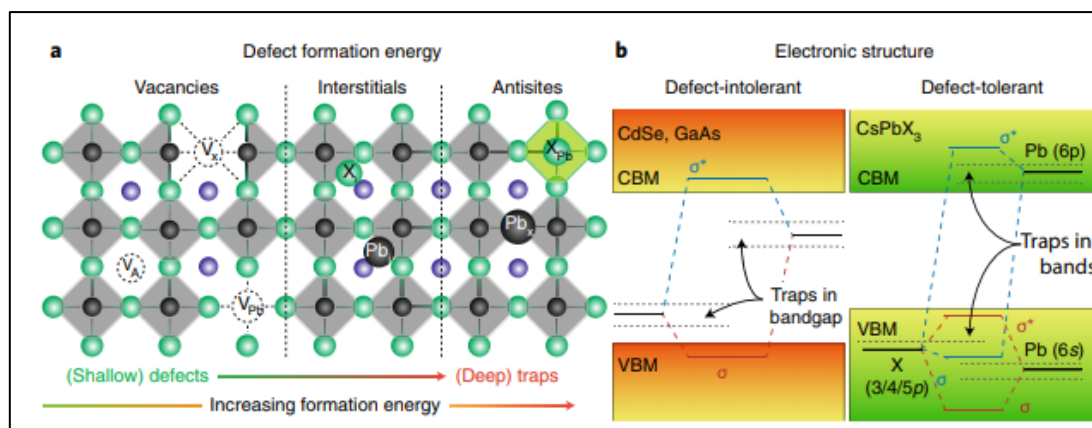


Figure 1.4: Main factors contributing to the defect-tolerance of LHP NCs. **a.** Typical point defects (vacancies, interstitials and antisites) in order of increasing formation energy and depth of the states that they form in the bandgap (vacancies form shallow states; interstitials and antisites form deep traps). **b.** Schematic representation of electronic band structure of conventional (defect-intolerant) semiconductors and LHPs (defect-tolerant). In defect-intolerant semiconductors, the bandgap is formed between bonding (σ) and antibonding (σ^*) orbitals, while in LHPs the bandgap is formed between two antibonding orbitals. ^[9]

1.2.4 Structural and Thermal lability

Structural and thermal lability are two major challenges for LHP NCs. As well stated, LHP NCs are formed as easy as they brake. This feature renders LHP NCs prone to lose their colloidal and structural integrity during isolation, purification and handling. CsPbBr₃ NCs are usually terminated by oleylammonium bromide or oleylammonium carboxylate. The ligand-binding of LHP NCs is highly dynamic causing a ligand dissociation with subsequent NC dissolution (**Figure 1.5**).^[10] Thermal instability is another important challenge which arises again from ligand detachment and thermal decomposition of LHP NCs (MAPbI₃ at around 150-200 °C and FAPbI₃ at around 290-300 °C) and renders LHP NCs highly prone to sintering. ^[9]

The challenges of structural and thermal instability have concerned the community and a lot of effort has been placed recently on the development of various post and during synthesis methods to improve the surface passivation of LHP NCs and make them more structurally and thermally stable. Such successful methods are summarized into three main strategies: (i) the addition of new ligands, (ii) the application of post synthetic, passivation treatments, and (iii) the embedding of NCs into various host matrices. A combination of the strategies (i) and (ii) is used to produce robust CsPbBr₃ NCs employed in this thesis as the active material of the distributed feedback Bragg (DFB) grating.

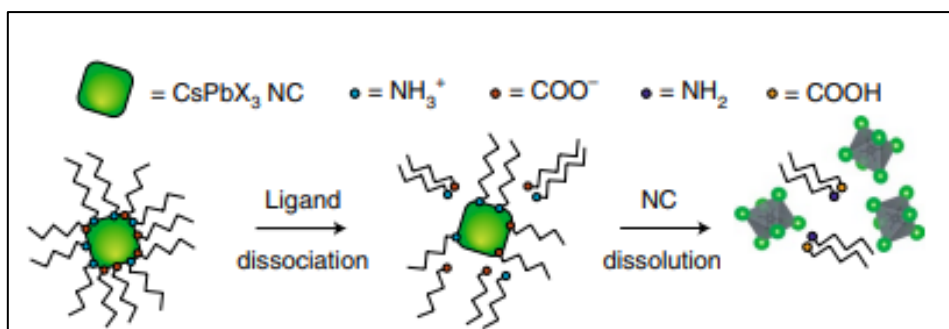


Figure 1.5: Structural lability of LHP NCs. The desorption of weakly and dynamic bound ligands leads to loss of colloidal stability and structural integrity of LHP NCs. ^[9]

CsPbBr₃ NCs were selected as they exhibit several advantages, with respect to their hybrid organic-inorganic counterparts, which render them appropriate and promising candidates for light-emitting applications (such as LEDs and lasers). The most important feature of the particular type of CsPbBr₃ NCs used, is their improved stability and long-term colloidal integrity due to the implementation of a newly developed ligand strategy involving didodecyldimethylammonium bromide (DDAB) ligands. The approach involves also, passivation with PbBr₂ subsequent to the synthesis of the DDAB-capped NCs, that has been found to efficiently passivate and heal defects of the 3D perovskite lattice of the NCs. Furthermore, CsPbX₃ NCs exhibit higher melting points and higher PL QYs compared to the hybrid organic-inorganic NC counterparts.

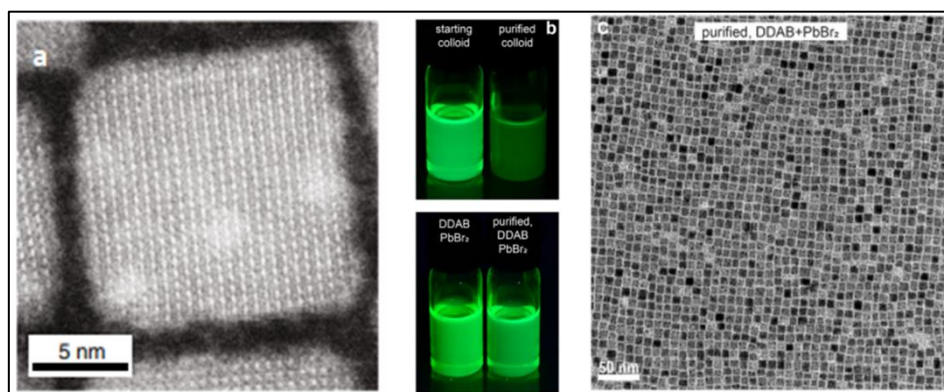


Figure 1.6: **a.** Scanning transmission electron micrograph (STEM) of a cubic CsPbBr₃ NC. ^[9] **b.** The top photograph shows the starting colloid which is synthesized using oleylamine (OLA) and oleic acid (OA) ligands before and after purification, and the bottom photograph shows the colloid treated with a mixture of DDAB + PbBr₂ before and after purification. The brightness of the starting colloid after purification is clearly lower than the brightness of the colloid treated with DDAB + PbBr₂. ^[11] **c.** TEM image of NCs with DDAB + PbBr₂ after purification, indicating the retention of structural integrity. ^[11]

1.3 Stimulated Emission

Stimulated emission is a radiative process by which an incoming photon can interact with an excited state electron, forcing it to lose a part of its energy by emitting a photon of the same frequency, polarization, phase and direction as the incident photon. The difference with the spontaneous emission is that stimulated emission occurs after the triggering by the photon field and results in photon emission with the specific characteristics mentioned above, while spontaneous emission occurs randomly in time and the emitted photons are incoherent and non-directional. The process characteristics and its relationship to the other fundamental processes of light-matter interaction, namely light absorption, and spontaneous emission, are governed by the Einstein's relations, discussed in the next section. Stimulated emission is the main process in which a laser is based.

1.3.1 Fundamental processes of light-matter interaction

If a photon hit an atom at ground state, the photon will be absorbed and cause the transition of the atom to a higher-energy state. This is the process of absorption (**Figure 1.7 a**). The rate of absorption is given by the relation (1.1):

$$\frac{dN_1}{dt} = -B_{12}N_1\rho \quad (1.1)$$

where B_{12} is Einstein's coefficient, N_1 is the number of atoms at the lower-energy state and ρ is the energy density. The energy density ρ , represents the number of photons which have sufficient energy for the transition between the lower and higher energy levels.

If an atom is in an excited state and a photon with energy E equal to the difference between the excited and the ground state comes along, it can simulate the atom to emit a photon. The emitted photon will have the same wavelength and phase with the incident photon and thus, this process will give two photons. This process is called stimulated emission (**Figure 1.7 b**). The rate of stimulated emission is given by the following relation:

$$\frac{dN_2}{dt} = -B_{21}N_2\rho \quad (1.2)$$

where B_{21} is Einstein's coefficient, N_2 is the number of atoms at the upper-energy state and ρ is the energy density.

In the process of spontaneous emission (**Figure 1.7 c**), an atom in an excited state emits a photon simultaneously without a triggering effect (in contrary with the absorption and stimulated emission where a photon initiates the process). The relation (1.3) gives the rate of spontaneous emission:

$$\frac{dN_2}{dt} = -A_{21}N_2 \quad (1.3)$$

where A_{21} is Einstein's coefficient for spontaneous emission and N_2 is the number of atoms at the upper-energy state.

The relation between the spontaneous radiative lifetime of the excited state τ , and the Einstein's coefficient for spontaneous emission A_{21} , is:

$$\tau = \frac{1}{A_{21}} \quad (1.4)$$

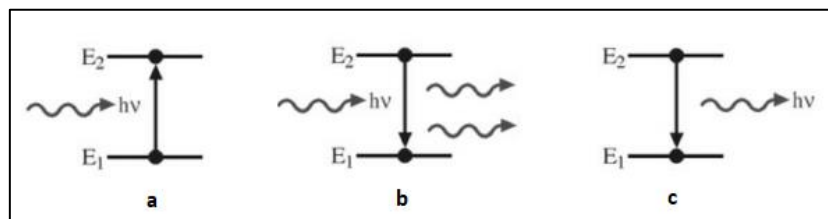


Figure 1.7: Fundamental processes of light-matter interaction. **a.** Absorption process. **b.** Stimulated emission. **c.** Spontaneous emission. ^[12]

The process of stimulated emission is a light amplification process, and the amplified light is coherent, monochromatic and collimated, so it has the three properties of the light which emitted by a laser. However, the atom which emits a photon in the process of stimulated emission, loses its energy so it must be excited again. This is the reason why another process, the population inversion, is required for the laser action to occur. When the population of atoms at a higher energy state is greater than the population of a lower energy state, the population inversion is achieved. For the achievement of population inversion, a higher rate of stimulated emission (relation 1.2) than the rate of absorption (relation 1.1) is required by the active material. ^[34]

1.3.2 Amplified Spontaneous Emission (ASE)

Through the process of amplified spontaneous emission (ASE), spontaneous emitted photons are amplified by stimulated emitted photons. The necessary condition for ASE to occur is that the optical gain of a medium must be higher than the respective light propagation losses, that are associated with light scattering, absorption and emission. The optical gain determines the ability of a medium to amplify photons by stimulated emission. We can say then that a material shows a net optical gain (net modal gain) when the rate of the stimulated emission is greater than the loss rates of spontaneous emission and absorption. The ASE peak appears typically at the wavelength range where the optical gain is maximum, and results in preferential amplification of this wavelength region of the spontaneous emission.

The capability of a material to show net optical gain that leads to light amplification is the main characteristic which renders that material promising candidate for lasing applications. The ASE peak in the photoluminescence spectrum of a material, gives information for the wavelength where the maximum optical gain is observed.

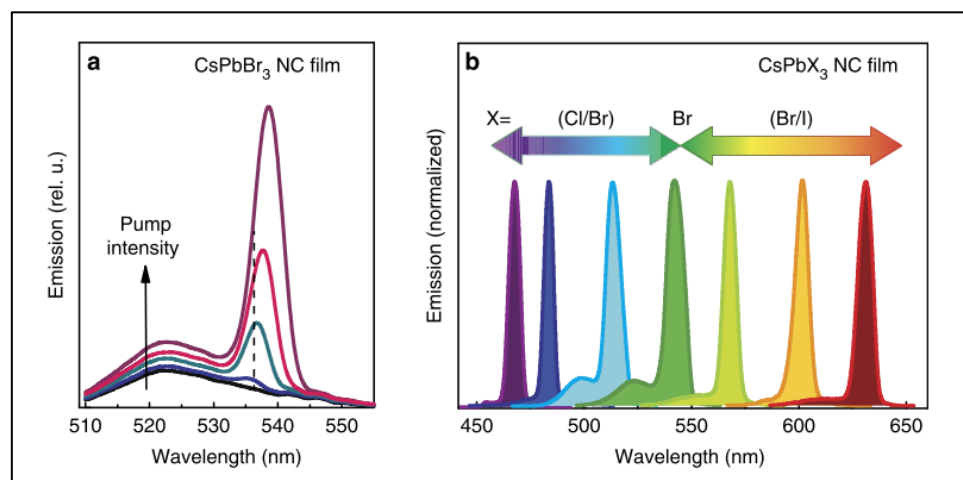


Figure 1.8: **a.** Excitation energy density dependence of the PL spectra of $CsPbBr_3$ NC thin film. For low excitation energy densities ASE peak is not observed. The ASE peak appears when the excitation energy density is high enough to create optical gain larger than the losses (net optical gain larger than zero). **b.** ASE tunability over the entire visible spectrum by compositional modulation of the $CsPbX_3$ NCs. ^[13]

1.4 Introduction to optical resonators

An optical resonator is a structure which creates a feedback mechanism that increases the optical path of the light propagating in an optical gain medium. All cavity resonators have resonant wavelengths which are discrete. The fact that resonant wavelengths are discrete, arises from the fundamental boundary condition of the light in the cavity which imposes that the amplitude and the phase of light must remain unchanged after a round-trip in the optical cavity. ^{[14],[15]}

The most common types of cavity resonators are Fabry-Perot, whispering gallery mode (WGM), distributed Bragg reflector (DBR), and distributed feedback Bragg (DFB) cavities. Fabry-Perot cavity is the simplest optical resonator, consisting of two mirrors and the optical gain medium between them (**Figure 1.9 a**). The WGM cavity is a dielectric cavity, with the shape of a sphere, disk, or ring, containing the gain material (**Figure 1.9 b**). DBRs are mirrors that are formed by alternated thin films of different dielectric materials. ^[16] These materials have a refractive index contrast, and thus they create a periodic modulation of the refractive index in the DBR. A DBR cavity typically comprises two DBRs and the active material between them (**Figure 1.9 c**). DFB cavities are divided into 1D, 2D and 3D structures. Typically, a 1D DFB cavity comprises a grating and a gain material (**Figure 1.9 d**).

In this thesis, DFB cavity resonators have been used due to some distinct features and advantages that possess, with respect to the other types of resonators, described in the next section.

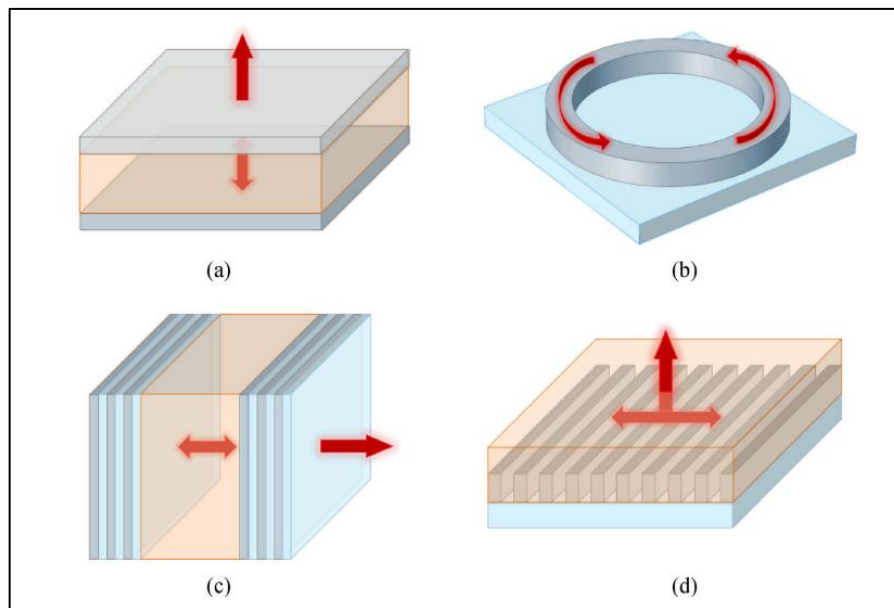


Figure 1.9: Different types of cavity resonators. **a.** Fabry-Perot cavity. **b.** Whispering Gallery Mode (WGM) cavity. **c.** Distributed Bragg Reflector (DBR) cavity. **d.** Distributed Feedback Bragg (DFB) cavity. ^[14]

1.4.1 Distributed Feedback Bragg (DFB) resonators

Distributed feedback Bragg (DFB) resonators consist of periodic nanostructures, which backscatter photons due to the periodic modulation of refractive index across the propagation direction of light. At the light wavelengths that fulfil the Bragg's law (Eq. 1.5), constructive interference of the backscattered photons occurs when:

$$m\lambda = 2n_{eff}\Lambda \quad (1.5)$$

where m is the diffraction order, λ is the light wavelength, n_{eff} is the effective refractive index of the waveguiding medium and Λ is the grating period. ^{[17],[18]}

The periodic modulation of the refractive index in DFB resonators is achieved with the fabrication of periodic gratings. The periodic gratings can be produced on a substrate and afterwards deposit the active film on the patterned substrate (**Figure 1.10 c**). Another way to realize a DFB resonator is by using a stamp with a periodic pattern to imprint it to the top surface of the film, after the deposition of the active material (**Figure 1.10 a, b**).

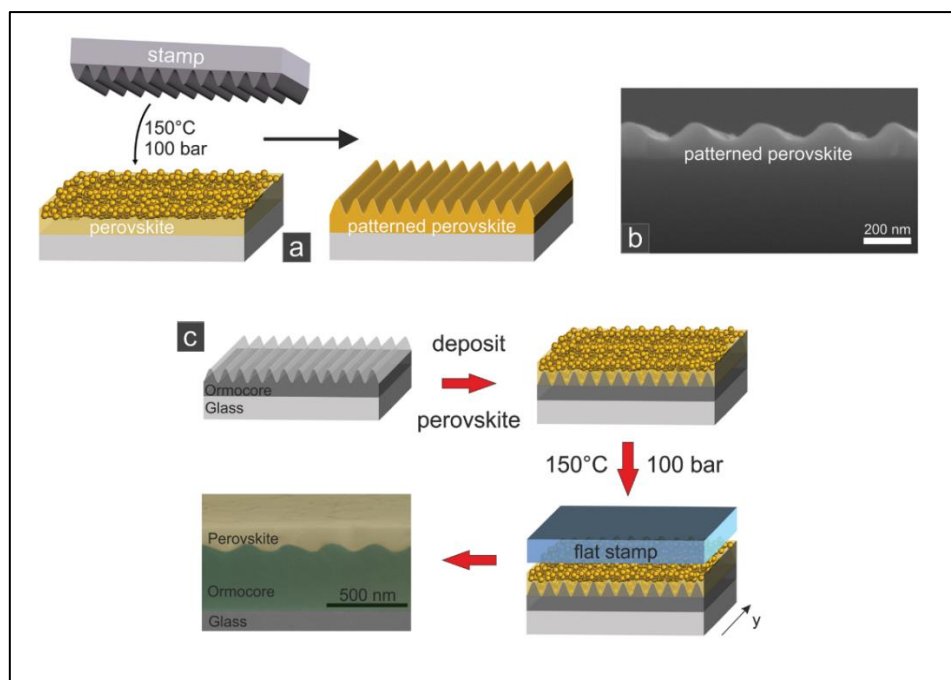


Figure 1.10: **a.** Schematic diagram of thermal imprint of a stamp with periodic line pattern on a perovskite layer which is deposited on a glass substrate. **b.** Scanning electron microscopy (SEM) image of the cross-section of the patterned perovskite layer. **c.** Schematic diagram of the procedure used to realize a DFB laser on a prepatterned layer. Glass substrates coated with a polymer resin (Ormocore) were patterned using a diffraction grating. The perovskite layer was coated on top of the prepatterned substrates and a flat silicon stamp was used to recrystallize and flatten it by thermal imprint. ^[19]

The partial reflection of light due to the refractive index variation, creates a feedback mechanism which is distributed along the periodic structure. This feedback mechanism is an important characteristic for the realization of a DFB laser.

DFB lasers that operate with first-order diffraction are side emitting, while second-order DFB lasers are both surface and side emitting. This behavior can be explained by dipole interference if the gratings are considered as arrays of dipole elements. The distance between two adjacent grating grooves is $\lambda_{eff}/2$ for first-order gratings and λ_{eff} for second-order gratings, according to Bragg's law, where $\lambda_{eff} = \lambda/n_{eff}$. For first-order gratings, the light path difference between counter-propagating waves, is a multiple integer of λ_{eff} (integer of 2π phase shift) due to reflection of the light at each refractive index variation. The result is constructive interference in the light propagation direction. At the perpendicular to the surface direction, the scattered light waves from two adjacent dipoles have a light path difference equal to $\lambda_{eff}/2$ and a subsequent π phase-shift, thus in this direction destructive interference occurs. In the case of second-order DFB gratings, the light path difference between two waves is $2\lambda_{eff}$, and thus there is also constructive interference in the light propagation

direction. Additionally, in this case constructive interference occurs in the perpendicular to the surface direction because the scattered waves are in phase. ^[20]

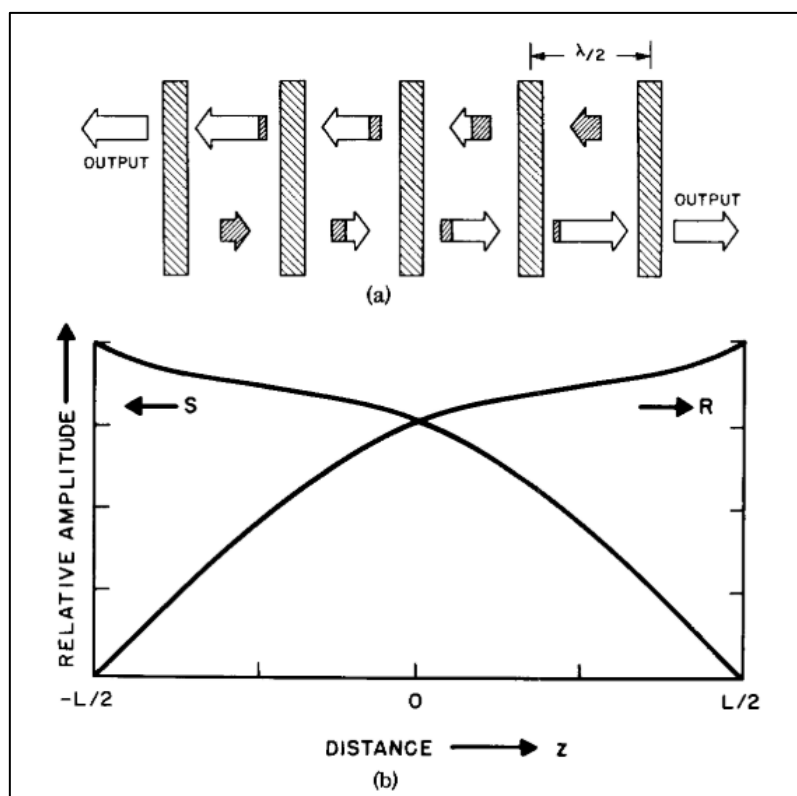


Figure 1.11: (a) Schematic diagram of a first-order DFB laser oscillation. (b) Relative amplitudes of left traveling wave $S(z)$ and right traveling wave $R(z)$. ^[21]

The operation of a first-order DFB laser is demonstrated in **Figure 1.11 (a)**. At each grating line, a part of the incident light is transmitted, and a part is reflected, resulting in a feedback mechanism. Thus, the electromagnetic field can be decomposed to a left and a right-propagating waves with amplitudes $S(z)$ and $R(z)$, respectively. The amplitudes of the two counter-propagating waves along the grating length (z -direction) are shown in **Figure 1.11 (b)**. ^{[20],[21]}

Coupled wave theory^[21] predicts that the wavelength that exactly satisfies Bragg's law cannot propagate in the film. This results to the formation of a photonic stopband centered at λ_{Bragg} , and the DFB laser oscillates on a pair of wavelengths, which are the wavelengths at the two edges of the photonic stopband. ^{[15],[22]} The mode at the smaller wavelength, exhibits a maximum in the center of the laser cavity due to constructive interference between the left and right-propagating waves. In contrast, the larger wavelength mode exhibits a minimum in the laser cavity center due to a π phase-shift between wave amplitudes, $S(z)$ and $R(z)$, resulting to destructive interference. This mode has a lower threshold in second-order DFB lasers. The reason is that surface radiation leads to an extra loss

with magnitude proportional to the optical intensity. Thus, the larger wavelength mode which exhibits a minimum in the cavity center, has smaller radiation loss and consequently smaller threshold. ^[20]

DFB resonators present several advantages with respect to other types of resonators. First, DFBs can provide narrow single mode emission with linewidths smaller than 1nm. Second, they typically show low lasing thresholds, which means that the required excitation energy for lasing operation is low. The low thresholds arise from the efficient increase of optical path length due to the consecutive reflections of the light inside the DFB resonator. Third, DFBs can be realized by relatively low-cost methods and they have the potential to be integrated with other devices. ^[22]

2. Experimental Methods

2.1 Film Deposition

Spin coating, dip coating and drop casting are common deposition methods used for processing into the solid state, solution-processed materials such as the colloidal NCs. For the film preparation in this project, the spin coating method was used as it can produce quite uniform thin films with thickness of the order of nanometers to micrometers. The film thickness depends mainly on two factors, the spin speed, and the viscosity of the solution. Other factors that can affect the thickness of the film are spin time, solution density, solvent evaporation rate, and surface wettability. ^[23] The following equation shows the different parameters that can affect the thickness of the layer,

$$h = \left(1 - \frac{\rho_A}{\rho_{A_0}}\right) \left(\frac{3\eta m}{2\rho_{A_0}\omega^2}\right)^{1/3} \quad (2.1)$$

where h is the layer thickness, ρ_A is the density of volatile liquid, η is the viscosity of solution, m is the rate of evaporation, and ω is the angular speed of the substrate. The equation (2.1) shows that for higher angular speeds of the substrate, the thickness of the film will be lower. ^[24]

The process of spin coating can be divided into four main stages, which are deposition, spin-up, spin-off, and evaporation of solvents (**Figure 2.1**). In the initial stage of deposition, solution is cast onto the substrate. The deposition of the solution can take place when the substrate is stationary (static spin coating) or when the substrate is already spinning (dynamic spin coating). The solution spreads on the substrate due to centrifugal force. In the next stage (spin-up), the substrate reaches the desired rotation speed and most of the fluid is expelled from the substrate. Afterwards, stable fluid outflow (spin-off stage) takes place. In this stage the fluid thins, and this thinning behavior is dominated by viscous forces. Finally, fluid outflow stops, and thinning is dominated by evaporation of the solvent. The result is a thin film of solid material on the substrate. ^[25]

The advantages of spin coating technique are that film thickness can be easily controlled by altering the rotation speed, and it results in reasonably thin and uniform films. In addition, spin coating is a low cost and fast operating technique. Spin coating has also some disadvantages, which are the difficulty to create multilayer structures and the difficulty to spin large substrates at a sufficiently high rate to create a thin film.

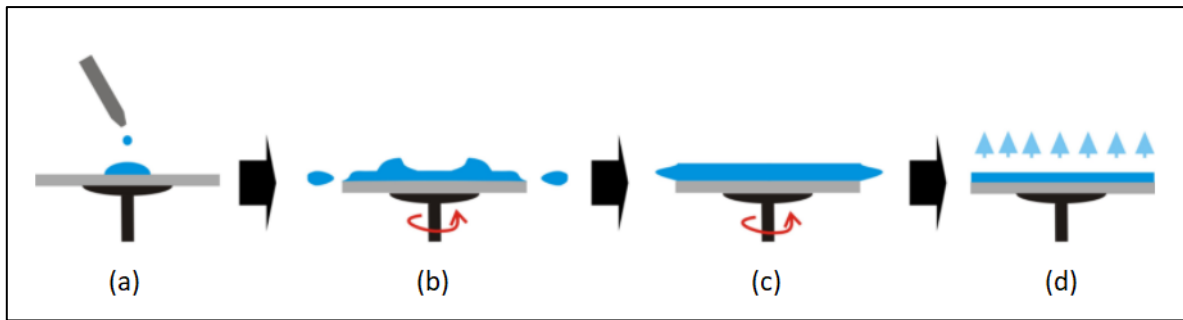


Figure 2.1: The four main stages of spin coating process. **(a)** Deposition, **(b)** spin-up, **(c)** spin-off, and **(d)** evaporation. ^[26]

2.2 Optical Modelling

FDTD simulator was used in order to simulate the DFB resonator with CsPbBr₃ NCs as the active material. The software used (FDTD Solutions, Lumerical) is based on the finite-difference time-domain method used to solve Maxwell's equations in complex geometries. Using Fourier transformations, FDTD can also provide frequency solutions, that can be used for the calculations of quantities such as the transmission and reflection of light. The mesh used by the FDTD, is rectangular in cartesian coordinates and the simulation quantities, such as the material properties and the electric and magnetic fields, are calculated at each point of the mesh. Decreasing the mesh size, the accuracy of the device representation increases. ^[35]

The aim of the simulations was to investigate the impact of different resonator parameters, on the wavelength, linewidth and intensity of the resonances observed, in order to obtain the optimal combination of these parameters to feed the experimental work. In addition, simulations enabled us to predict the properties of the photonic structures. The parameters that were investigated, are the grating period, the height of the grating grooves and the active material thickness.

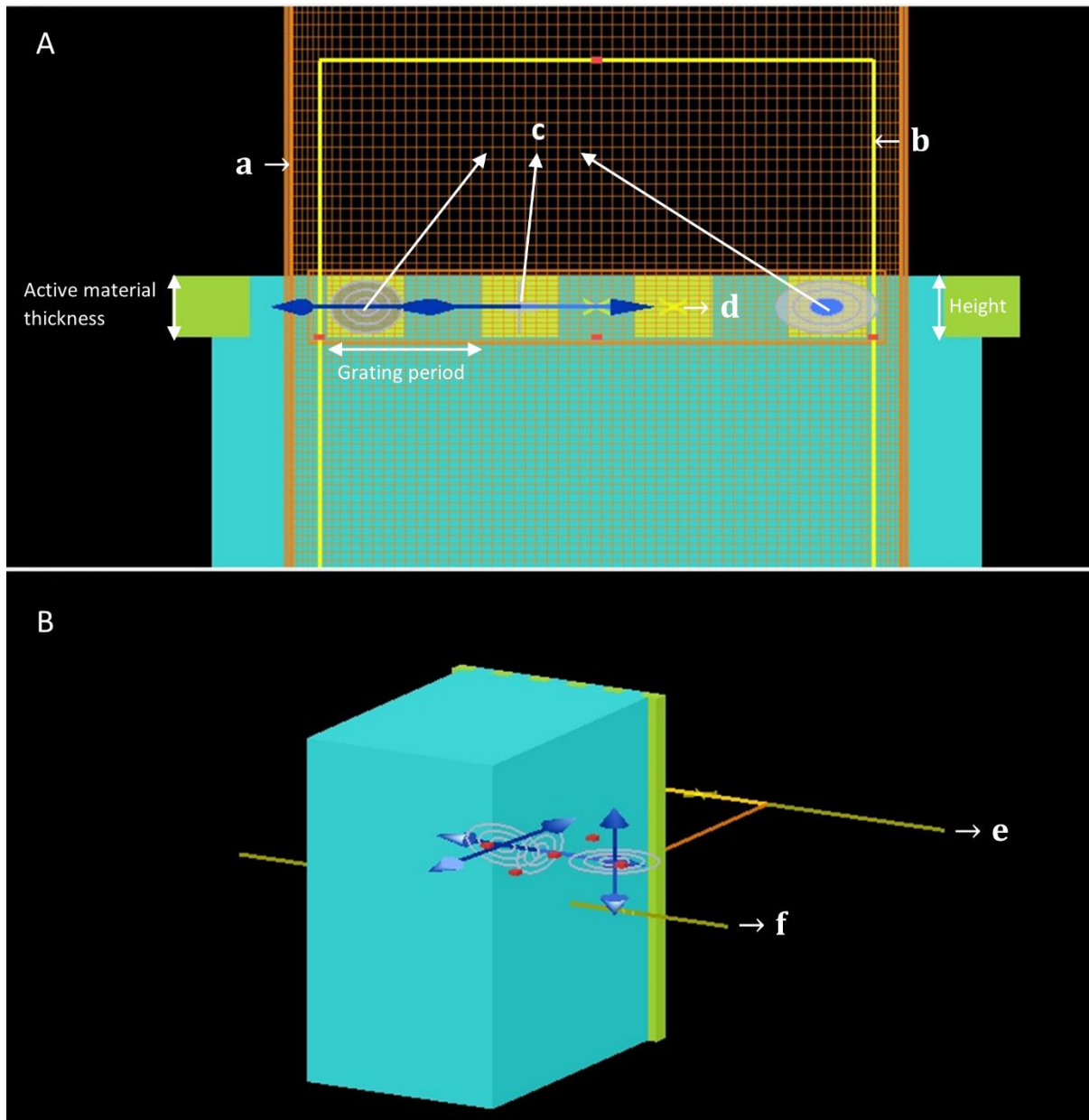


Figure 2.2: Schematics of the simulation of the DFB grating. **A.** Cross-section of DFB grating. **a.** Simulation region, **b.** monitors to extract the profiles of the electric and magnetic fields of the resonances, **c.** dipoles with random orientations in the active material region (green region), **d.** time monitor that measures the electric and magnetic fields over time. **B.** Perspective view of the DFB. **e, f.** Monitors used to measure the reflection and transmission spectra, respectively.

2.3 Spectroscopic Techniques

2.3.1 Absorption Setup

The absorption of a light beam by an optical medium is described by the Beer-Lambert law,

$$I(z) = I_0 e^{-az} \quad (2.2)$$

where $I(z)$ is the intensity of the transmitted light through a material in the z direction, I_0 is the optical intensity at $z=0$, and a is the absorption coefficient of the optical medium. The absorption coefficient is a function of wavelength, and thus an optical medium can absorb only a specific light wavelength across the electromagnetic spectrum.

The absorption of an optical medium can also be quantified in terms of the optical density O.D. which is given by the following relation,

$$O.D. = -\log\left(\frac{I(z)}{I_0}\right) \quad (2.3)$$

The relation between the absorption coefficient and the optical density can be found by combining the equations (2.2) and (2.3),

$$O.D. = \frac{az}{\log_e(10)} = 0.434az \quad (2.4)$$

For the measurement of the optical density (O.D.) of the samples, a PerkinElmer Lambda 1050 Spectrophotometer was used (**Figure 2.3**). The spectrophotometer consists of a deuterium light source which emits from 200 nm – 320 nm (UV range), and a tungsten halogen light source which emits in the range of 300 nm – 3250 nm (UV/Visible and NIR). The light of these sources is analysed by a double grating monochromator and then a common beam mask adjusts the beam size so that O.D. of samples of different dimensions can be detected. Afterwards, a common beam depolarizer corrects the inherent instrument polarization for more accurate measurements. The light beam then passes through a chopper with four-segment design. The four parts of the chopper are: a mirror, two black parts, and a blank part. The mirror reflects the light beam so light passes only through the sample. The two black parts do not allow the light to pass through the sample and reference sample, thus no light reaches the detectors and background signal is recorded. The last part of the chopper is blank and allows light beam to pass only through the reference sample so that the reference signal can be recorded. Finally, three high sensitivity detectors measure the transmitted light. The detectors are, a photomultiplier tube (PMT) that covers the range from 250 nm – 850 nm, an InGaAs detector for the range of 850 nm – 1700 nm, and a PbS detector for the range of 1700 nm – 3000 nm.

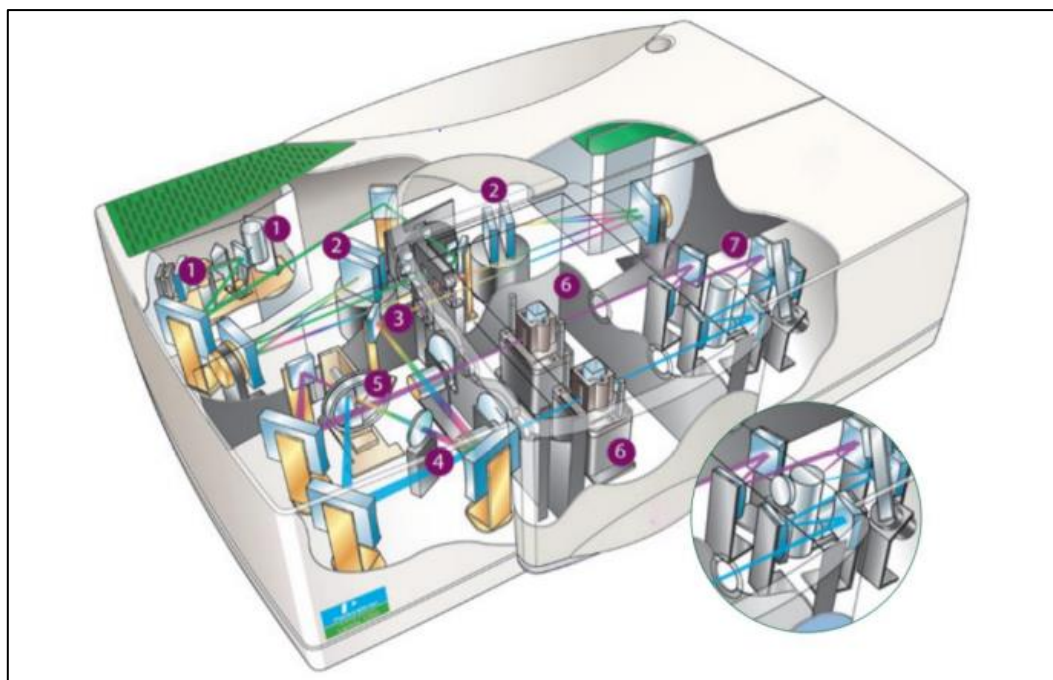


Figure 2.3: Illustration of PerkinElmer Lambda 1050 spectrophotometer. (1) Deuterium (200 nm – 320 nm) and tungsten-halogen (300 nm – 3250 nm) light sources. (2) Double grating monochromators for high analysis. (3) Common beam mask that enables precise adjustment of the light beam height. (4) Common beam depolarizer corrects the inherent instrument polarization for accurate measurements. (5) Chopper with four-segment design. (6) Sample and reference holders. (7) High sensitivity detectors: Photomultiplier tube (PMT) that covers the range of 250 nm – 850 nm, InGaAs detector which detects from 850 nm – 1700 nm, and PbS detector for the range of 1700 nm – 3000 nm. ^[27]

2.3.2 Photoluminescence Setup

Photoluminescence (PL) is a radiative emission process in solids, that occurs after the absorption of a photon. The optical excitation of a material leads to absorption of photons with energy equal to or larger than the energy gap E_g of the material, with subsequent injection of electrons to the conduction band and holes to the valence band. The excited electrons lose their energy by emitting phonons, and then they relax to the bottom of the conduction band. With the same way the holes relax to the top of the valence band. Subsequently, electrons and holes recombine radiatively, by emitting photons, or non-radiatively.

Photoluminescence spectroscopy has different approaches based on the parameters that are varied during the PL measurements. Steady state PL spectroscopy is used to measure the spectrum of a material, and in this case the wavelength of the excitation source (typically a laser or monochromatic light from a lamp) is fixed. In PL excitation spectroscopy (PLE), the detecting wavelength is fixed, and the excitation wavelength is varied producing a spectrum that is analogous to the absorption of the

material. Another PL spectroscopy method is the time-resolved PL (TRPL) spectroscopy. In TRPL spectroscopy a short light pulse from a laser is used to excite the sample, and the emission spectrum is recorded on a fast detector as a function of the time after the arrival of the pulse. TRPL gives information about relaxation processes and recombination mechanisms of the carriers and measures the PL lifetimes.^[36]

A widely used method to measure PL lifetimes is the time-correlated single photon counting (TCSPC) method. Using TCSPC method the determination of PL lifetimes in the range of picoseconds to microseconds can be achieved. The method is based on the approximation that the number of the detected photons at a specific time is proportional to the PL intensity at this time. For the excitation of the sample a pulsed source is used. The first single photon emitted, after a laser pulse, is detected and a histogram of the detected photons as a function of the photon arrival times (the time difference between the laser pulse and the first emitted photon) is formed. For the detection of the single photons, photomultiplier tubes (PMTs) are typically used. PMTs amplify the weak signal that single photons cause so it can be detected.^[28] The data of the histogram can be fitted by single or multiexponential decay curves and the average PL lifetime can be calculated from the relation (2.5),

$$\tau_{av} = \frac{\sum_i A_i \tau_i^2}{\sum_i A_i \tau_i} \quad (2.5)$$

where τ_i are the decay times extracted from multiexponential fits and A_i are the corresponding decay amplitudes.

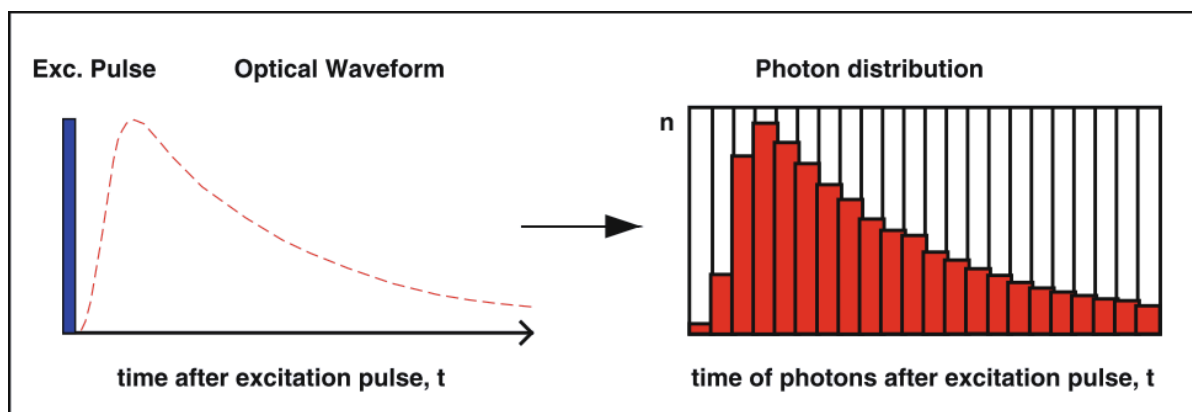


Figure 2.4: TCSPC method. Detected signal of electrons that emitted after laser pulses. Each point corresponds to a bin of the photon distribution histogram.^[29]

A typical setup for PL measurements is illustrated in **Figure 2.5**. A light source, that can be a continuous wave (CW) or pulsed laser or a lamp combined with a monochromator, is used to excite the sample. The placement of the sample in a cryostat enables the variation of the temperature of the sample (temperature-dependent PL) and it can also lead to reduction of the interactions with phonons when

the sample temperature is low. A monochromator analyses the light emitted by the sample and send it to the detector.

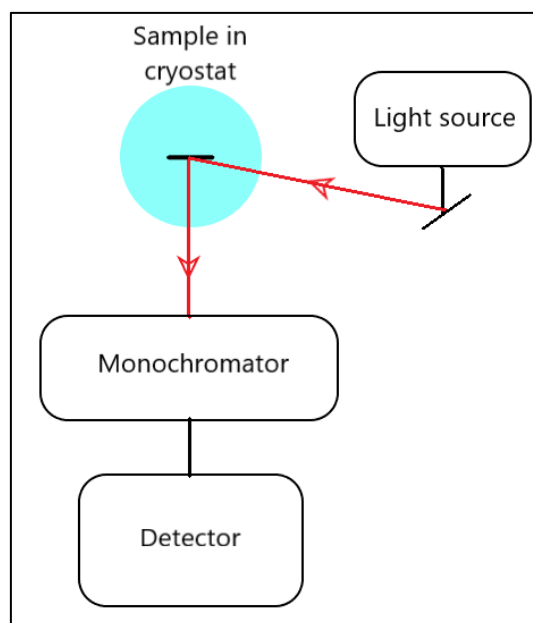


Figure 2.5: Schematic diagram of a typical PL setup.

For the purpose of this thesis two experimental setups for the investigation of steady state PL and TRPL were used. A compact Ocean Optics spectrometer was used to record steady state PL spectra and a FluoroLog FL3 Horiba spectrophotometer was employed for both steady state and time-resolved PL measurements.

The Ocean Optics spectrometer is illustrated in **Figure 2.6**. Light from an optical fiber enters the spectrometer (**Figure 2.6 (1)**). A slit (**Figure 2.6 (2)**) controls the amount of light entering the spectrometer and the spectral resolution and then a filter (**Figure 2.6 (3)**) restricts the light to pre-determined wavelength regions. Subsequently, the light is focused on a grating via a collimating mirror (**Figure 2.6 (4)**). The grating (**Figure 2.6 (5)**) diffracts the light that is collected by another mirror, (**Figure 2.6 (6)**) which directs the light on the detector plane via a collection lens (**Figure 2.6 (7)**) that focuses the light onto the detector to increase the light-collection efficiency. The detector (**Figure 2.6 (8)**) is a CCD array that converts the optical signal received from the detector collection lens to digital signal, and it is responsive in the range of 200 nm – 1100 nm. Finally, linear variable filters LVF (**Figure 2.6 (9)**) can be used for effective separation of the excitation and emission. ^[30]

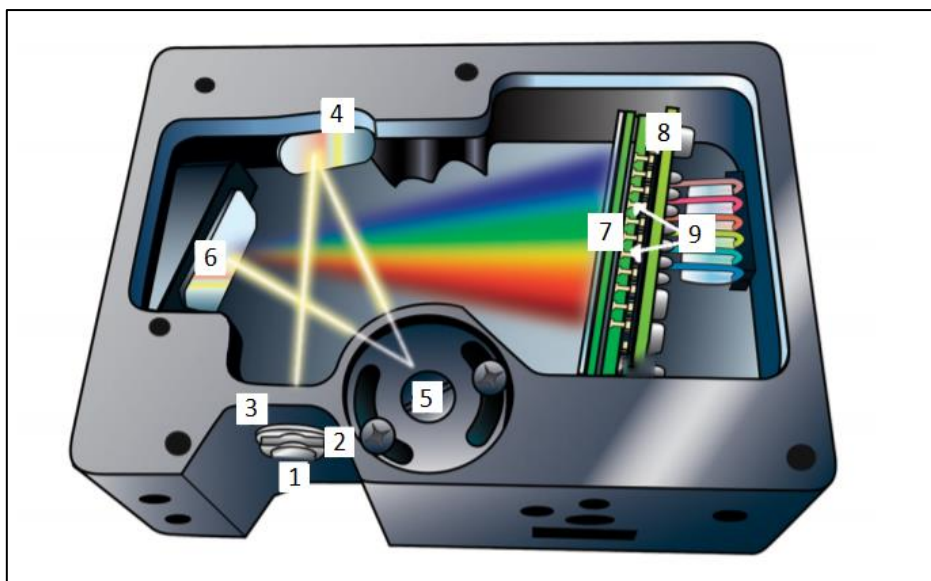


Figure 2.6: Illustration of the Ocean Optics spectrometer. Components of the spectrometer: (1) Connector for the optical fiber, (2) slit, (3) filter, (4) collimating mirror, (5) grating, (6) focusing mirror, (7) detector collection lens, (8) detector (CCD array) and (9) linear variable filters (LVF). [30]

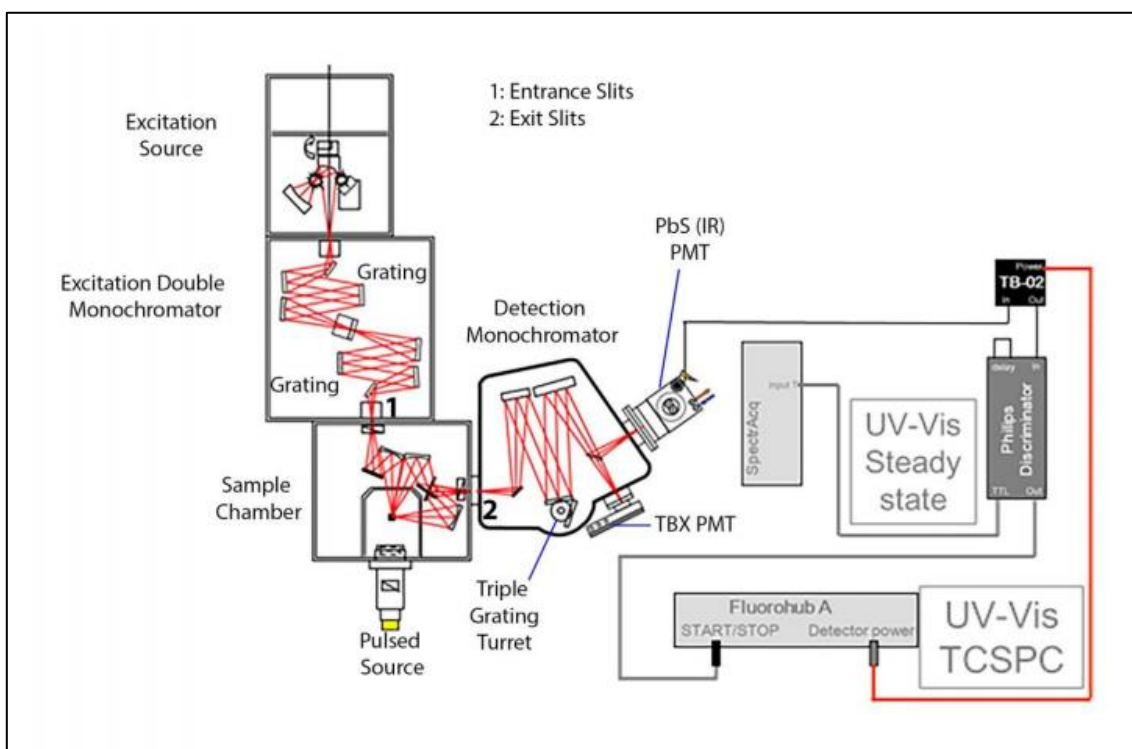


Figure 2.7: Illustration of the FL3 Horiba spectrophotometer. [reprinted from manual]

A schematic diagram of the FL3 Horiba spectrophotometer is shown in **Figure 2.7**. The light of an ozone-free xenon (O_3 free Xe) arc lamp emitting from 250 nm to 2500 nm, is analysed via a double monochromator that uses two gratings. The double monochromator provides high resolution single wavelength light that excites the sample which is placed in the sample chamber. The emitted light from the sample enters a detection monochromator which includes a turret with 3 gratings. The grating used in this work has 1200 grooves/mm and center wavelength at 500 nm and sends the light in a visible TBX PMT (250 nm – 850 nm) to be measured. For TRPL measurements the setup is the same, but the excitation source is a pulsed laser, and electronics such as a preamplifier and a photon counting system are used. In the TCSPC mode, the setup exhibits a time-resolution of the order of 100 ps in the visible spectral range.

2.3.3 Optical microscope setup

A typical microscope setup comprises an excitation light source, which is a laser or a lamp with an excitation filter, a dichroic mirror, a barrier filter, a microscope objective lens, and a detector. The light source excites the sample resulting to emission from the sample. A commonly used configuration in fluorescence microscopes is epi-illumination. In this approach, the excitation of the sample is performed through the microscope objective. The emitted light from the sample reaches to the detector through the same microscope objective, leading to an overlapping of the excitation and emission in the light path. The dichroic mirror is used to separate the excitation from the emission, and also a barrier filter is used to prevent the excitation light from reaching the detector. ^[31]

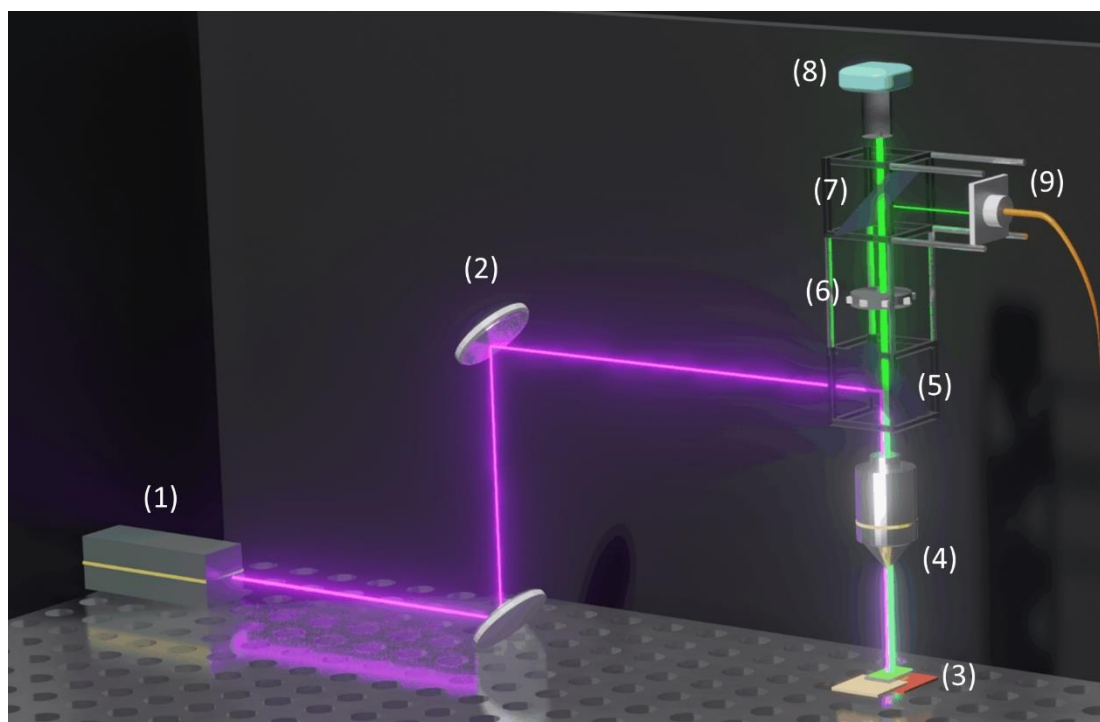


Figure 2.8: Illustration of the optical microscope setup used in this work. The components of the setup are: (1) 405 nm diode laser, (2) mirrors, (3) sample, (4) microscope objective lens (10x, 0.25), (5) dichroic mirror, (6) linear polarizer and long pass filter, (7) beam splitter, (8) CCD camera, and (9) multimode single core 100 μm fiber.

The optical characterization setup used in this thesis is illustrated in **Figure 2.8**. In the same setup steady state PL and TRPL measurements were performed. For the steady state PL, a linearly-polarized CW laser diode (**Figure 2.8 (1)**) emitting at 405 nm with output power set to 1 mW was used to excite the sample. The excitation of the sample and the collection of the emitted light were performed through the same microscope objective (10x, 0.25). A dichroic mirror (**Figure 2.8 (5)**) and a long pass filter (495 nm) were used to prevent the excitation light from reaching the camera and the fiber that was collecting the emitted light. In addition, a linear polarizer (**Figure 2.8 (6)**) was used to analyse the linear polarization of the emitted light from the sample. A beam splitter (**Figure 2.8 (7)**) was used to separate the emitted light and send the 50% of its intensity to the CCD camera (**Figure 2.8 (8)**), which was monitoring the sample surface, and the other 50% was detected via a multimode single core 100 μm fiber (**Figure 2.8 (9)**) and analysed via the aforementioned Ocean Optics CCD and FL3 Horiba spectrometers. For the TRPL measurements, a linearly-polarized pulsed laser diode emitting at 405 nm was used as the excitation source and the spectra were analysed via the FL3 Horiba spectrophotometer at TCSPC mode.

2.3.4 Angle-resolved Photoluminescence and Transmission setup

Angle-resolved PL and transmission measurements were performed in the setup illustrated in **Figure 2.9**. For the angle-resolved PL measurements, the linearly- polarized 405 nm CW laser diode was used as the excitation source. A linear polarizer was used to analyse the light emitted from the sample and a long pass filter (495 nm) was used to block the excitation laser light. Subsequently, a collimating and a focusing lenses were focusing the emitted light on a multimode single core 100 μm fiber. The collection of the emitted light via the fiber was performed at different angles of the goniometer (-30° to 30°) with 1° step. For the angle-resolved transmission measurements, a broad band tungsten-halogen white light source coupled into a 600 μm multimode core fiber was used. The white light was analysed via a linear polarizer and then focused on the sample in an approximately 2 mm spot diameter. The transmitted light was collected via a 100 μm multimode core fiber. All the measurements were analysed by the Ocean Optics spectrometer.

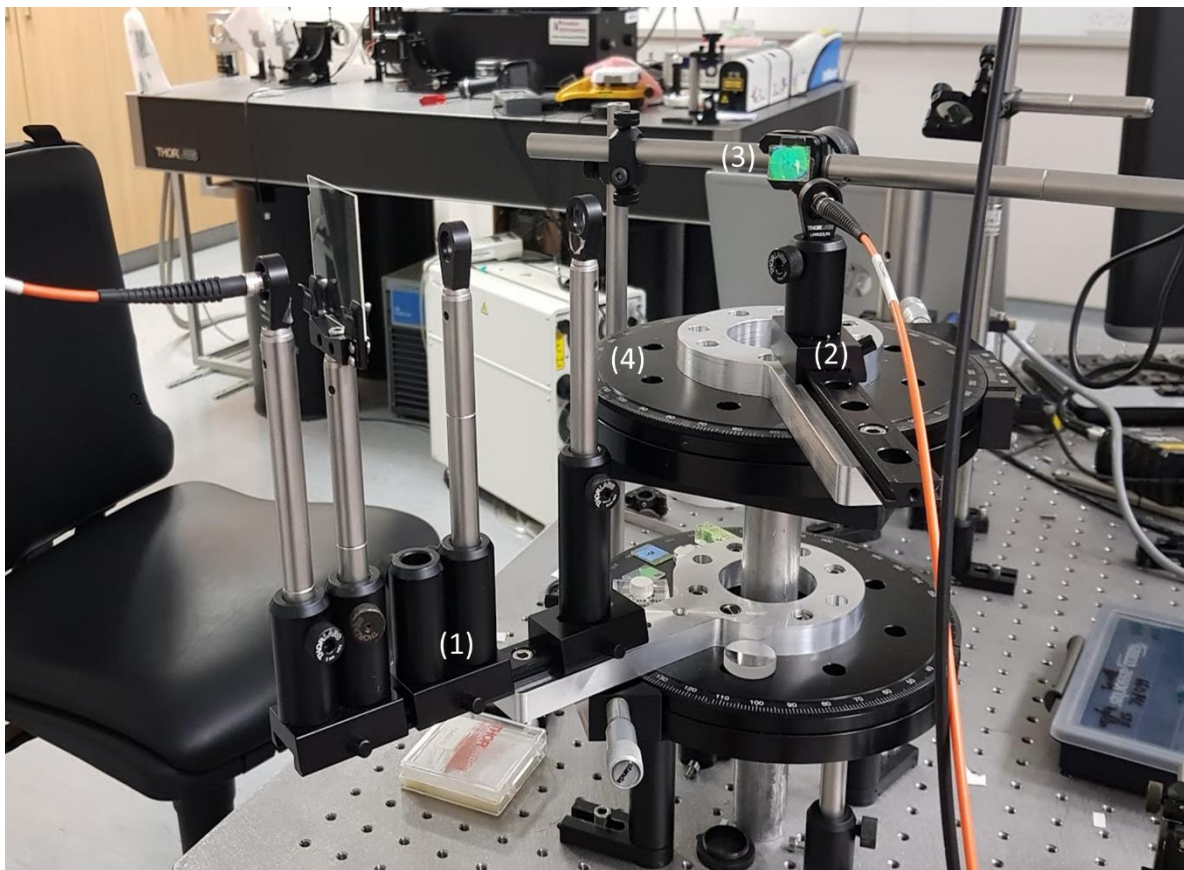


Figure 2.9: Illustration of the setup used for the angle-resolved PL and transmission measurements. **(1)** First setup arm with the following components: collimating and focusing lenses, linear polarizer, and long pass filter. Also, fiber for the collection of emitted light for PL measurements, or white light source coupled into fiber for transmission measurements. **(2)** Second setup arm with fiber for the collection of transmitted light. **(3)** Sample. **(4)** Goniometer.

3. Results and Discussion

3.1 Data Analysis

The steady state PL spectra were recorded while varying the angle of a linear polarizer to analyse the polarization of the emitted light upon two excitation cases: (i) with the linear polarization of the excitation laser set perpendicular and (ii) parallel to the grating grooves. For the analysis of the measurements, firstly, the background was removed from the recorded spectra by subtracting a spectrum that was recorded without the excitation source. Subsequently, all the measurements were divided by a correction factor to take into consideration the polarization degree of the system. For the calculation of the polarization degree of the light emitted from the samples under investigation, over the wavelength, the following equation was used:

$$P = \frac{I_{max} - I_{min}}{I_{max} + I_{min}} \quad (3.1)$$

where P is the polarization degree and I_{max} and I_{min} are the maximum and minimum PL intensities, respectively.

TRPL decay curves were plotted in semi-log axes and fitted using the following triple exponential model:

$$y = y_0 + A_1 e^{-x/t_1} + A_2 e^{-x/t_2} + A_3 e^{-x/t_3} \quad (3.2)$$

where t_1 , t_2 and t_3 are the decay lifetimes for each channel, and A_1 , A_2 and A_3 are the corresponding amplitudes. Using the values of A_i and t_i ($i=1,2,3$), the average PL lifetime was calculated by the relation (2.5).

In angle-resolved PL measurements, the background was removed from the spectra with the same process used in the steady state PL measurements. The collection of the emitted light from the sample was performed in different angles (off-normal direction), so Lambert's cosine law was used to correct the measured PL intensity. According to Lambert's cosine law, the radiant intensity observed from an ideal diffuse radiator is directly proportional to the cosine of the angle between the light direction and the surface normal. Thus, the intensity in all the angle-resolved PL data was corrected by dividing with the cosine of the angle, assuming a Lambertian emission profile.

3.2 Optical characterization of DFB gratings with CsPbBr₃ NC overlayers

The samples investigated in this thesis, are two types of DFB gratings with periods 278 nm and 416 nm, produced by nanoimprint lithography with cellulose diacetate (CdA) as the substrate. The gratings were provided by the collaborative group of J. Cabanillas-Gonzalez at IMDEA, Madrid. The procedure for the production of DFB gratings involves the imprinting of a Si DFB master mold onto a CdA film. CdA substrates were heated at 180 °C undergoing a pressure of 40 bar for 300 s, resulting in softening of CdA and filling of the mold grooves. Subsequently, the substrate was cooled down to 70 °C and the pressure was released, allowing removal of the imprinted substrate. ^[18]

CsPbBr₃ NCs were deposited onto the DFB gratings via spin coating. For both samples, 40 μL of the NC solution was spin coated on gratings at 1200 rpm for 30 seconds with a subsequent drying step at 2500 rpm for 10 seconds.

All the measurements were performed in two different excitation directions with respect to the grating grooves. In the case of perpendicular excitation, the polarization of the laser light was perpendicular to the grating grooves and parallel to the light propagation direction and thus parallel to the TM mode of the DFB grating. So, this case, corresponds to excitation of the TM mode. In parallel excitation the laser light polarization was parallel to the grating grooves and parallel to the TE mode of the grating, corresponding to excitation of the TE mode. The observed light diffraction on the sample, in both cases, was perpendicular to the grating grooves.

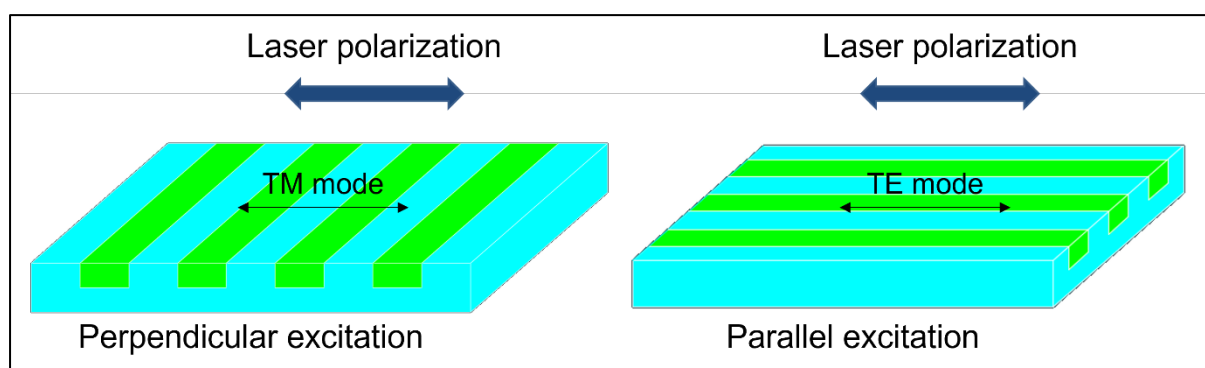


Figure 3.1: Perpendicular and parallel excitation configurations. Perpendicular excitation corresponds to excitation of the TM DFB mode, and parallel excitation to excitation of the TE DFB cavity mode.

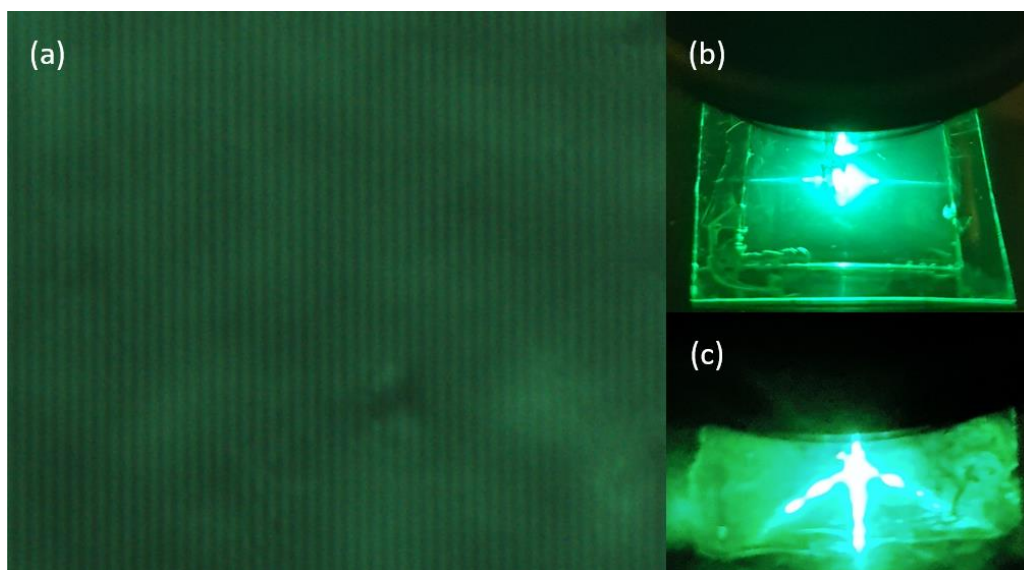


Figure 3.2: (a) Picture showing the grating lines of DFB grating with period $\Lambda=416$ nm coated with $CsPbBr_3$ NCs. (b), (c) Pictures of the samples where the diffraction pattern of DFB grating with $\Lambda=278$ nm and $\Lambda=416$ nm, respectively, can be seen. All the pictures show the case of perpendicular excitation of the samples.

In **Figure 3.3**, the absorption and PL spectra of a $CsPbBr_3$ NC film are illustrated. The PL peak position is at $\lambda \sim 519$ nm with a narrow emission line width of ~ 19 nm, as seen in the figure.

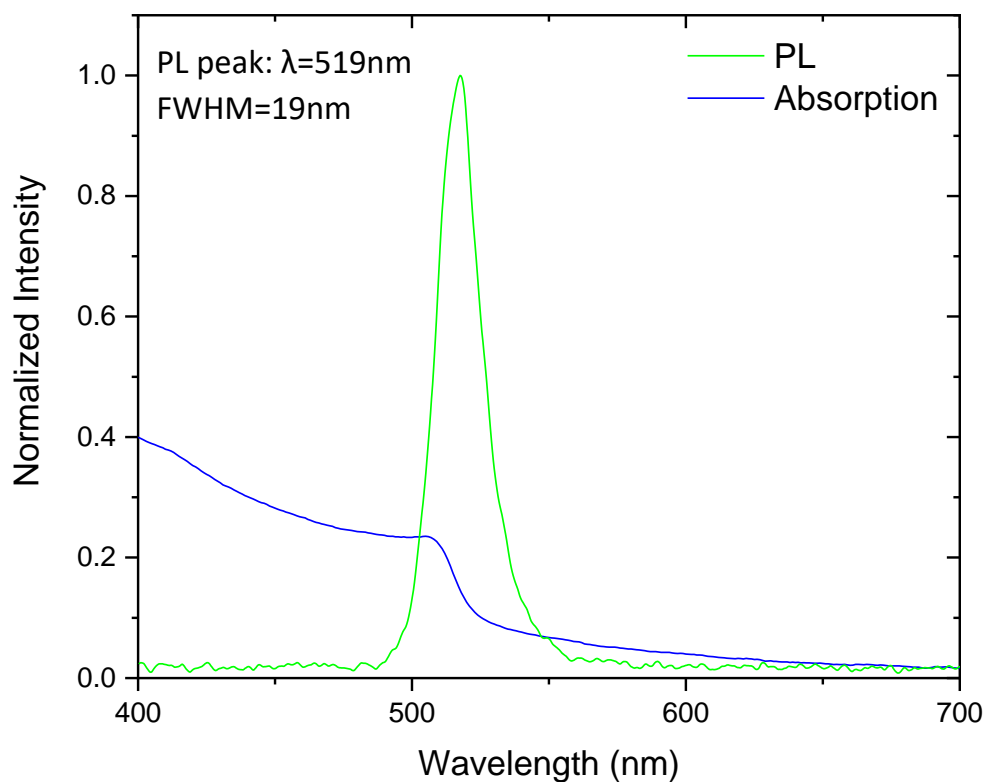


Figure 3.3: PL and absorption of a spin-coated $CsPbBr_3$ NC film.

3.2.1 Steady state photoluminescence measurements

Figure 3.4 comprises representative polarization-resolved PL spectra from CsPbBr₃ NCs deposited on the two different DFB gratings studied. The linear polarization of the excitation laser was set for each sample in the perpendicular and parallel configuration while the polarization of the emitted light was analysed within the 0° to 90° range. Each of the four cases are discussed further below.

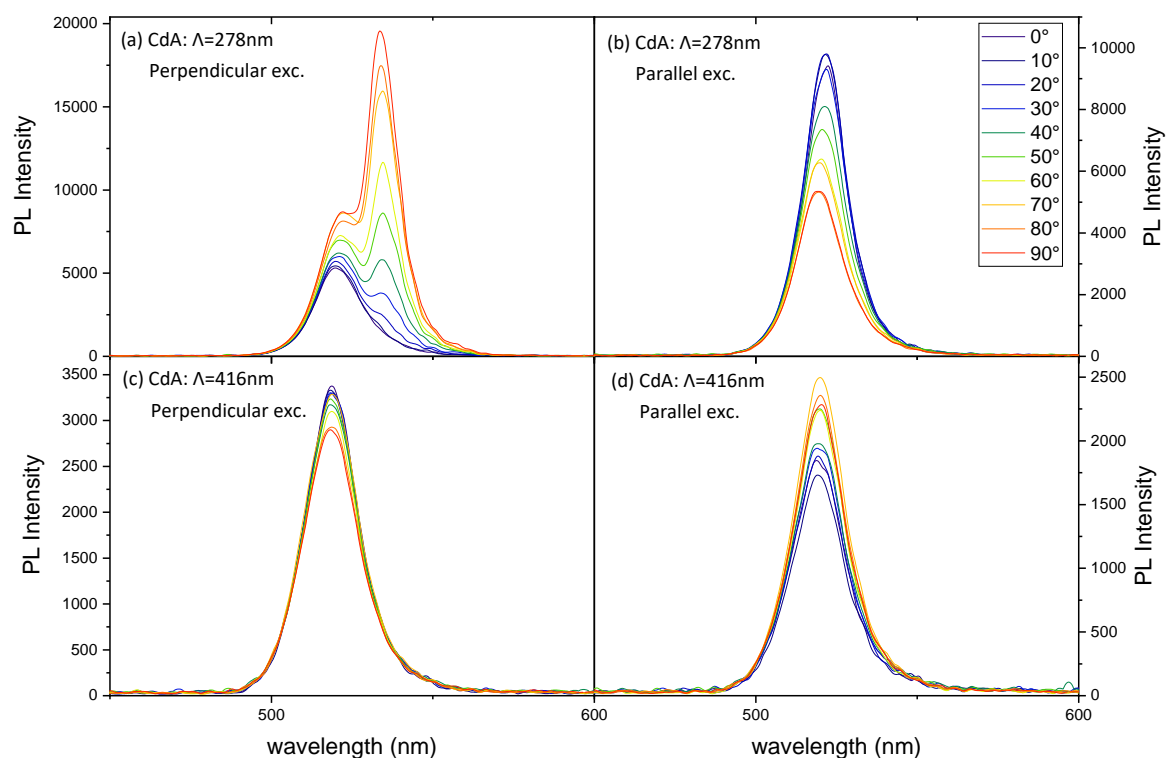


Figure 3.4: Polarization-resolved steady state PL spectra of the two DFB-NC samples. **(a), (b)** DFB grating with $\Lambda=278$ nm under perpendicular and parallel excitation, respectively. **(c), (d)** DFB grating with $\Lambda=416$ nm under perpendicular and parallel excitation, respectively.

(a) $\Lambda=278$ nm-Perpendicular excitation:

Two peaks are observed in the PL spectra (**Figure 3.4 (a)**), the first at $\lambda \sim 520$ nm which is the PL peak of the NCs in the absence of cavity, and the second at $\lambda \sim 534$ nm that is assigned to the coupling of a DFB cavity mode with the emission of the NCs. As expected, by varying the angle of the linear polarizer, the resonance can be controlled, being stronger for polarizer angle $\theta=90^\circ$ (parallel to the laser polarization direction, perpendicular to the grating grooves), while completely quenching for polarizer angle $\theta=0^\circ$ (perpendicular to the laser polarization direction, parallel to the grating grooves).

(b) $\Lambda=278$ nm-Parallel excitation:

In this case, the measurements show a polarization-dependent variation in the PL intensity, however the spectra contain no visible second peak as a result of the interaction of the NC emission with the cavity photonic modes. The above, indicate that the NC emission in such a case couples weakly to one of the cavity modes.

(c), (d) $\Lambda=416$ nm:

Significantly smaller induced changes are observed in the PL intensity and lineshape for the grating with $\Lambda=416$ nm in both excitation directions, as can be seen in the **Figure 3.4 (c), (d)**. This is anticipated and in agreement with the theory, as the wavelength where constructive interference occurs, based on the Bragg's law, for grating period $\Lambda=416$ nm, is not within the emission range of the CsPbBr₃ NCs (**Figure 3.3**).

Further analysis of the spectra recorded for the sample with $\Lambda=278$ nm in perpendicular excitation is shown in **Figure 3.5**. For polarizer angles 0° and 180°, the electric field component of the emitted light is perpendicular to the light propagation direction (TE modes). For such polarization, the PL signal is relatively weak and singly-peaked at the same position as the pristine NC emission, indicating that the NC PL couples rather inefficiently to the TE modes of the grating. In contrast, for polarizer angles 90° and 270° the PL intensity is significantly higher, and a strong, second emission peak is observed as a result of the coupling of the DFB mode with the NC emission. In this case, the emitted light is TM-polarized as the vector of the electric field is parallel to the propagation direction of light. These results indicate that there is sufficient coupling between the NC PL and the TM cavity mode.

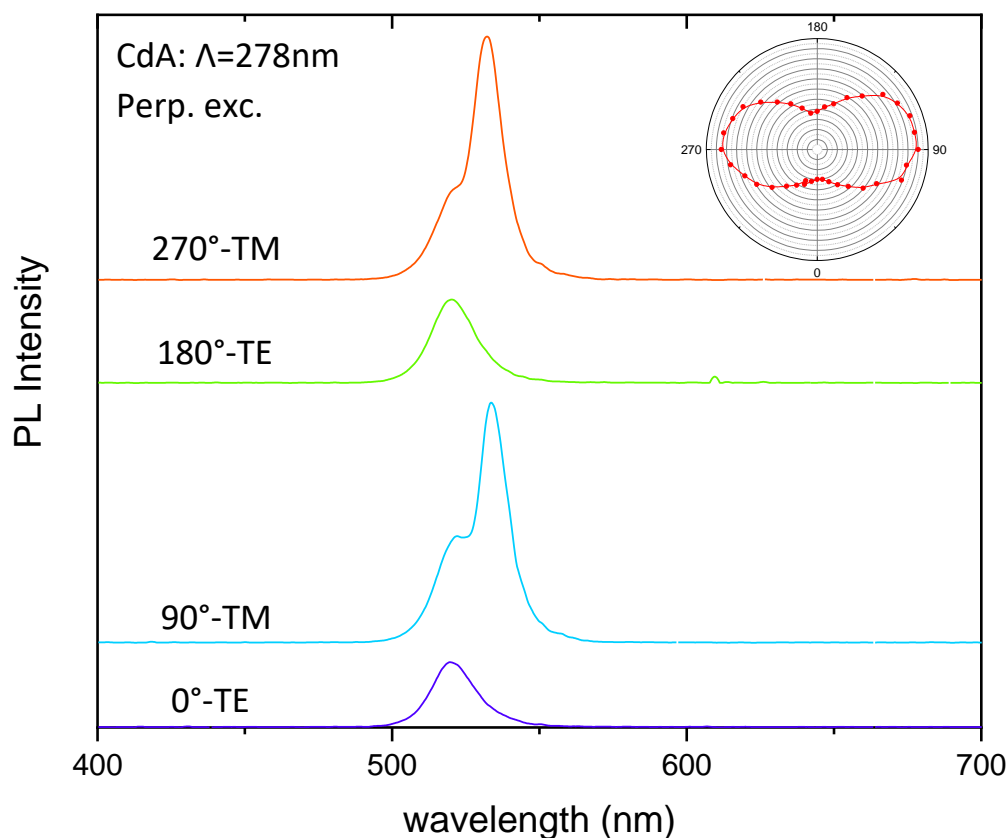


Figure 3.5: PL spectra for polarizer angles 0° , 90° , 180° and 270° . Inset shows the respective polar plot for angles from 0° to 360° .

Figure 3.6 (a) contains polar plots of the emitted light intensity from the samples for polarizer angles in the 0° - 360° range. The high degree of linear polarization in the emitted light for the case of the $\Lambda=278$ nm sample when the excitation laser polarization is perpendicular to the grating grooves, can be readily observed. The polarization degree of the emitted light, over the studied wavelength range is plotted in **Figures 3.6 (b)-(e)**. For the sample with $\Lambda=278$ nm, and perpendicular excitation, high linear polarization of the emission, up to $\sim 86\%$ at $\lambda \sim 537$ nm, can be obtained. The polarization degree for the resonance peak ($\lambda \sim 534$ nm) is only slightly lower ($\sim 84\%$) while it drops at the PL peak of the NCs ($\lambda \sim 520$ nm) at $\sim 20\%$. In parallel excitation of the same sample (**Figure 3.6 (c)**), the polarization degree is significantly smaller, being at a level of $\sim 26\%$ at $\lambda = 520$ nm and $\sim 27\%$ at $\lambda = 534$ nm. For the sample with $\Lambda=416$ nm, the polarization degree is lower than 15% in both excitation directions, and thus we can say that a negligible interaction of the NC emission with cavity modes exists. This result can be also confirmed from the polar plots in **Figure 3.6 (a)**.

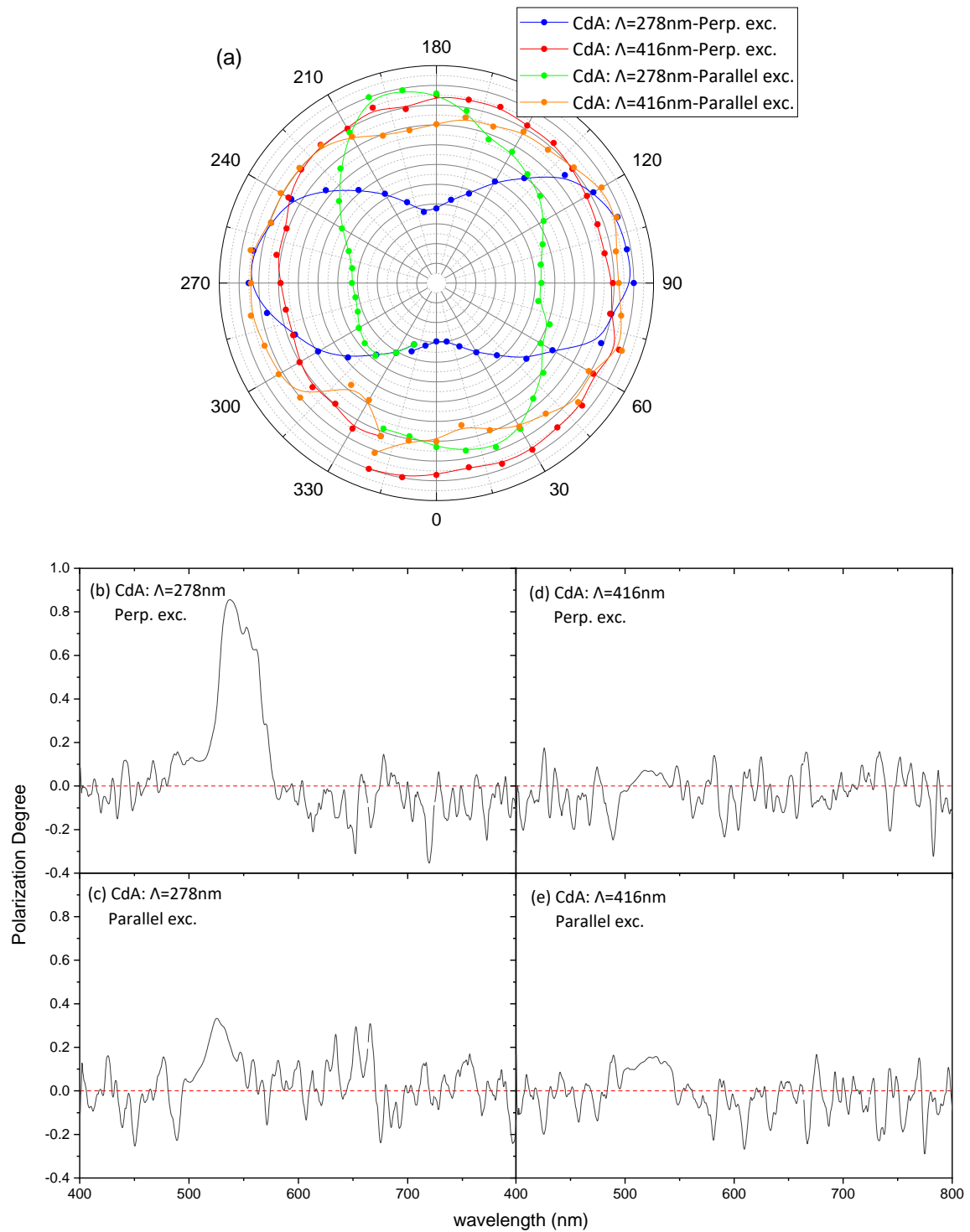


Figure 3.6: (a) Polar plots of the emitted light intensity from the samples for polarizer angles from 0° - 360° . (b)-(e) Calculated polarization degree over the wavelength for the two samples, with $\Lambda=278\text{ nm}$ and $\Lambda=416\text{ nm}$, in both excitation directions.

3.2.2 Time-resolved photoluminescence measurements

PL decay curves were recorded at two NC emission wavelengths: (i) the PL peak of the CsPbBr₃ NCs in the absence of a DFB cavity and (ii) the resonance mode wavelength, using the polarization configuration described before (i.e., laser polarization perpendicular or parallel to the grating grooves and polarizer angles of $\theta=0^\circ$ and $\theta=90^\circ$).

The PL decay curves for the two DFB gratings and a pristine NC film under perpendicular and parallel excitation are displayed in **Figure 3.7** and **Figure 3.8**, respectively. It can be observed that the average lifetime in all probed cases, almost doubles upon deposition of the NCs in the DFB grating structures compared to bare films deposited in glass. This is attributed to the different dielectric environment that the NCs experience in the two cases. It can be also observed that there are not significant differences in decay lifetimes between the two different angles of the linear polarizer for all the samples under investigation. This result indicates that: (i) there is no preferential orientation of the NC dipoles within the grating structure and (ii) the coupling of the NC emission with the cavity mode is not sufficiently strong to observe a modification of the radiative rate of the NCs (Purcell Effect). Importantly though, a polarization-dependent variation of the PL intensity is also present in the transient regime for the case of perpendicular excitation of the $\Lambda=278$ nm structure as seen in **Figure 3.7 (b)**. This is consistent with the steady state PL results, confirming the stronger coupling of the NC emitted light with the TM cavity mode.

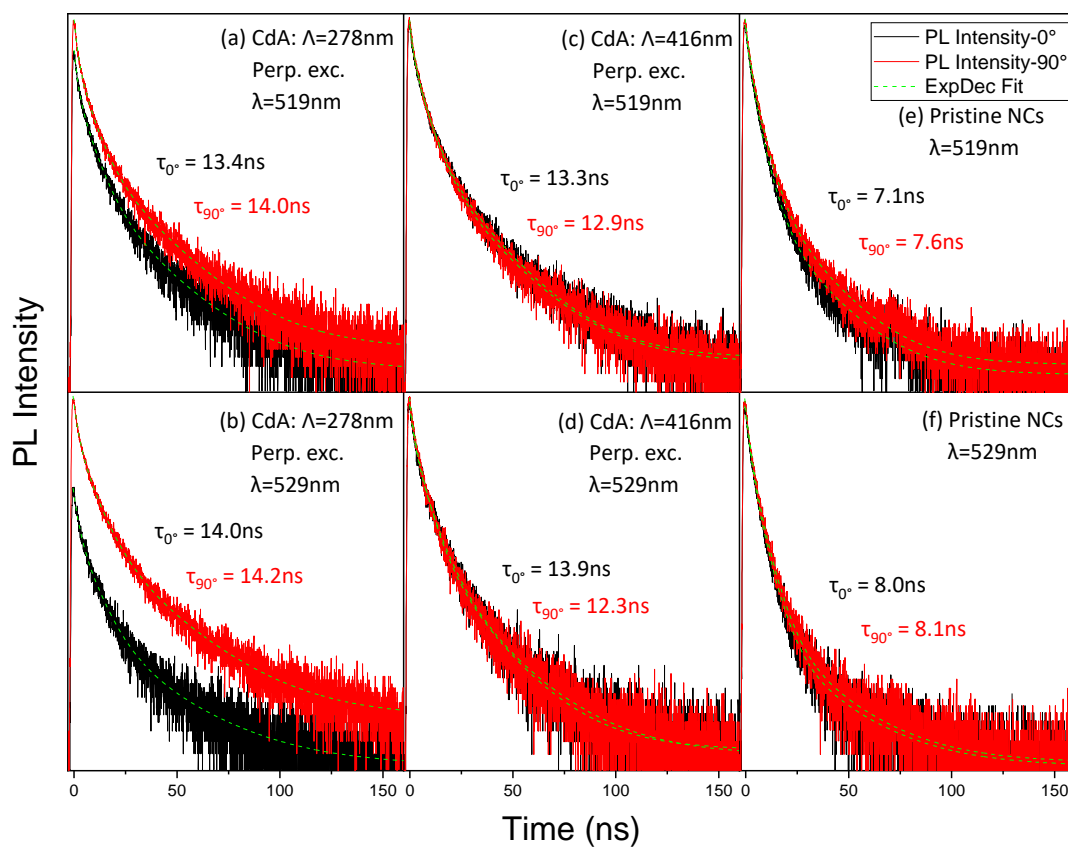


Figure 3.7: PL decay curves for perpendicular excitation of the two gratings and a pristine NC film at the emission peak of the NCs and the resonance wavelength. For each sample and wavelength, the PL decay curves were recorded for polarizer angles: $\theta=0^\circ$ and $\theta=90^\circ$. Also, the calculated average lifetimes are shown in the figure.

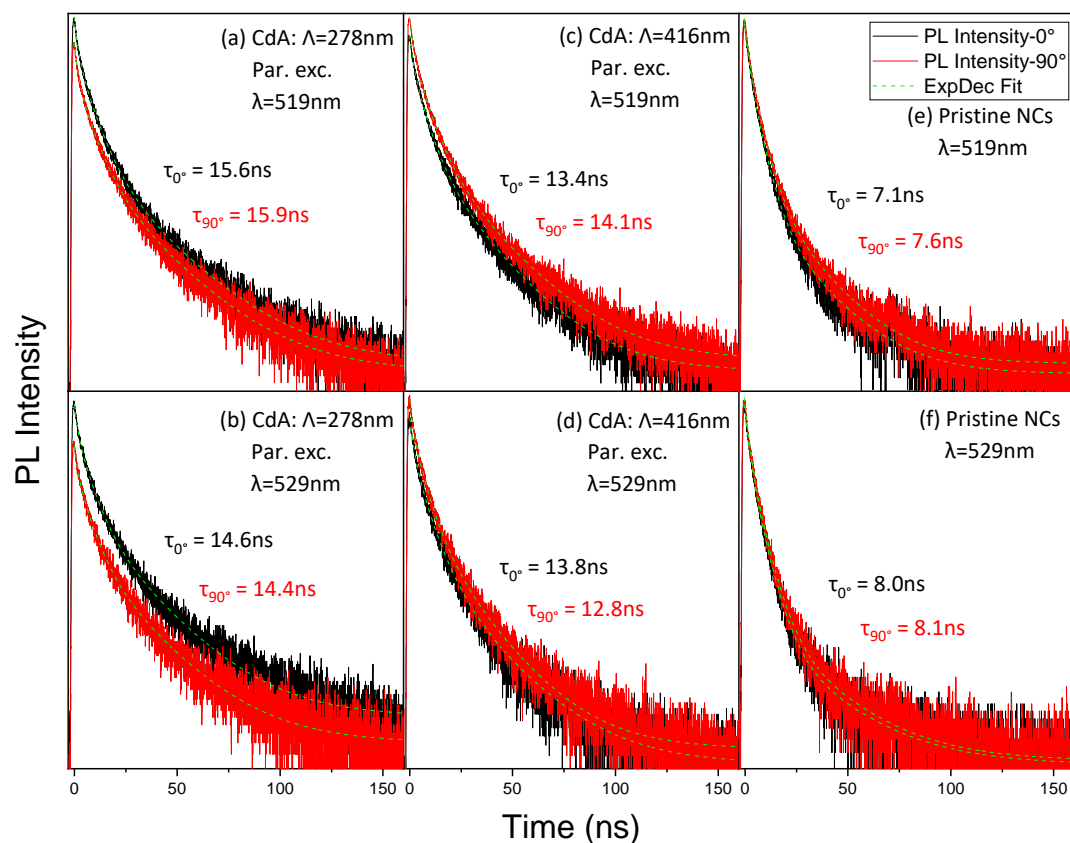


Figure 3.8: PL decay curves for parallel excitation of the two gratings and a pristine NC film at the PL maximum of the NCs and the resonance wavelength for polarizer angles 0° and 90° .

Using the PL decay curves, the polarization degree of the emitted light from the three samples was calculated via the relation (3.1). The results for the two probed emission wavelengths are displayed in **Figure 3.9**. For the sample with $\Lambda=278$ nm in the case of perpendicular excitation, the polarization degree is about 25% at the PL peak of the NCs ($\lambda=519$ nm), as seen in **Figure 3.9 (a)**. At the resonance wavelength $\lambda=529$ nm, a strong polarization of about 67% is observed (**Figure 3.9 (b)**), in agreement with the polarization degree measured in the steady state PL experiments ($\sim 66\%$). In the case of parallel excitation of the sample with grating period 278 nm, the polarization degree is $\sim 20\%$ at $\lambda=519$ nm (**Figure 3.9 (c)**) and $\sim 30\%$ at $\lambda=529$ nm (**Figure 3.9 (d)**). These results are also consistent with the corresponding polarization degrees obtained in the steady state regime.

The polarization degree for the sample with $\Lambda=416$ nm and the pristine NC film is below 10-15% for both excitation directions and detection wavelengths, confirming that the polarization results obtained for the sample with $\Lambda=278$ nm can be predominantly attributed to the coupling of NC emission with the DFB modes.

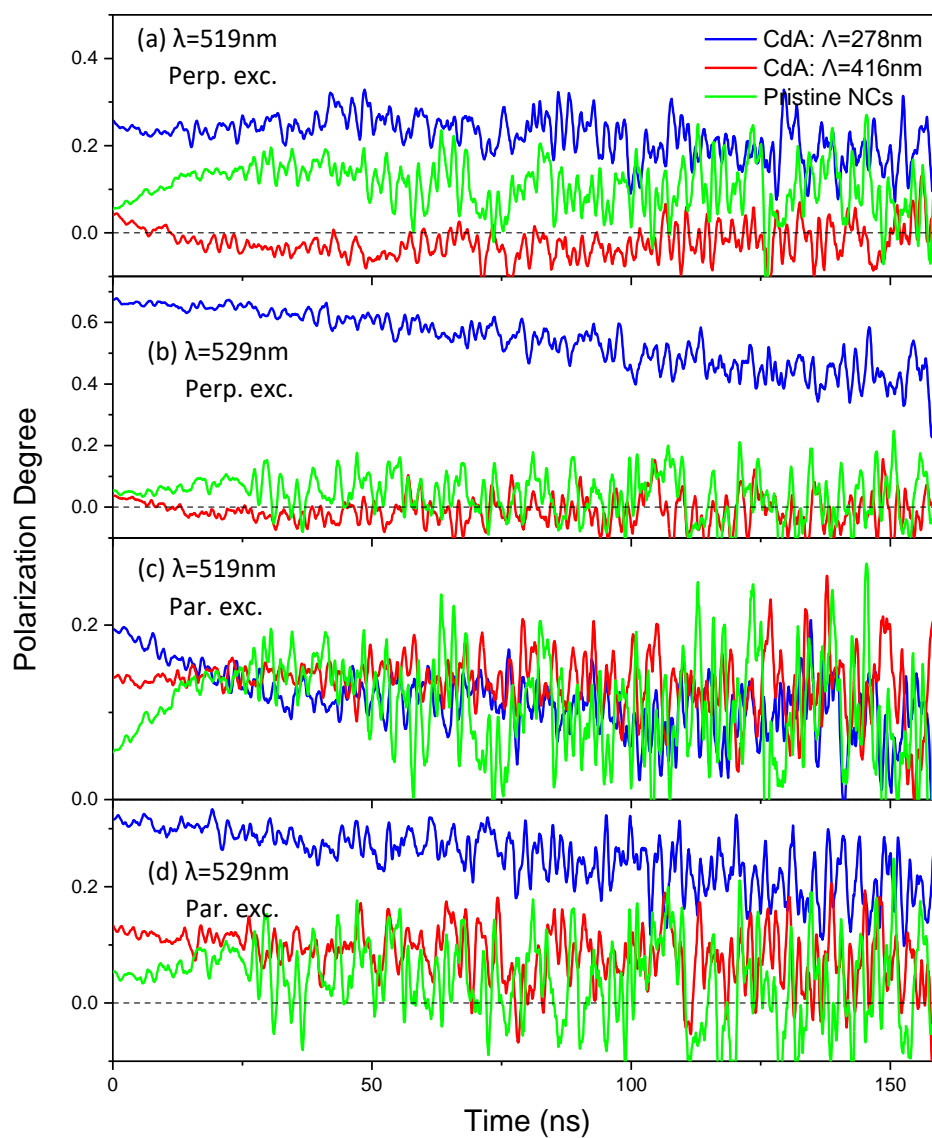


Figure 3.9: Polarization degree calculated via TRPL measurements. The figure illustrates the polarization degree for three different samples (DFB gratings with periods 278 nm and 416 nm and a pristine NC film) under perpendicular and parallel excitation at PL maximum of the NCs, $\lambda=519\text{ nm}$, and at the resonance wavelength, $\lambda=529\text{ nm}$.

3.2.3 Angle-resolved Photoluminescence and Transmission measurements

In order to investigate the photonic band structure of the DFB gratings in the presence of the CsPbBr₃ NC overlayers, angle-resolved PL and transmission measurements were performed. The data for the angle-resolved transmission are shown in **Figure 3.10**.

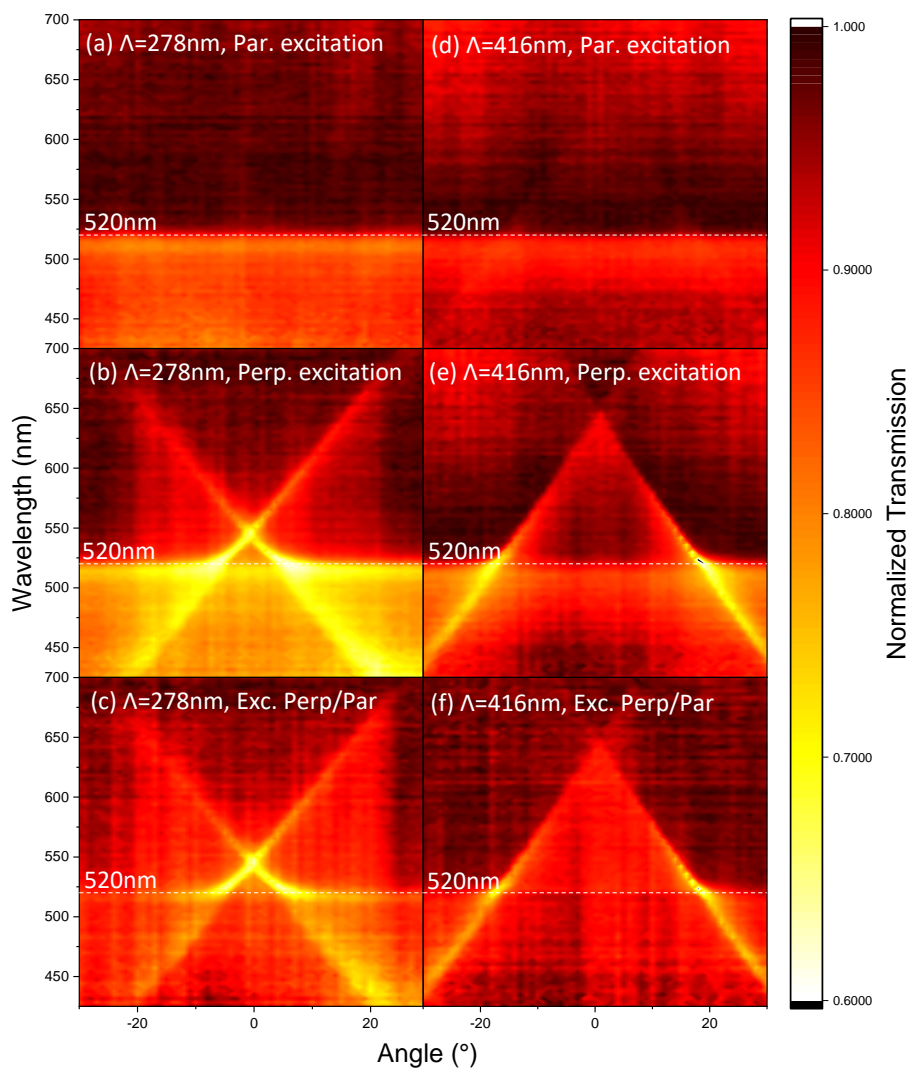


Figure 3.10: Angle-resolved transmission of the two grating samples.

Figure 3.10 (a) and **(d)** show the parallel excitation (which corresponds to excitation of the TE DFB mode) of the samples with $\Lambda=278$ nm and $\Lambda=416$ nm, respectively. From these two graphs, it is clear that the incident light is not coupled into the TE waveguide mode for the $\Lambda=278$ nm grating, while a weak interaction is visible for the $\Lambda=416$ nm grating. Thus, the observed modification of transmission is attributed only to the NC material. It can be seen that in both graphs the transmission is lower below 520 nm and it increases above 520 nm which is the band gap position of the NCs (see **Figure 3.3**).

The graphs in **Figure 3.10 (b)** and **(e)**, display the perpendicular excitation of the two DFB gratings (excitation of the TM waveguide mode). The graphs have two discrete bands that anticross at normal incidence. For the grating with $\Lambda=278$ nm, the two bands anticross at $\lambda\sim 546$ nm, while for $\Lambda=416$ nm the bands anticross at $\lambda\sim 650$ nm. The transmission through the samples at the two bands is low, due to scattering of the incident light into the TM DFB cavity mode. In **Figure 3.10 (c)** and **(f)**, the transmission measurements for polarizer angle $\theta=90^\circ$ (perpendicular excitation) were divided by the transmission measurements for $\theta=0^\circ$ (parallel excitation) to remove the effect of NCs on transmission and thus enhance the effect due to the photonic band dispersion.

To further understand the features in the photonic band dispersion in **Figure 3.10**, we can refer to the scattering processes leading to the coupling of incident light into waveguide modes. There are two main scattering processes involved: (i) first-order Bragg scattering that couples light into and out of the waveguide, and (ii) second-order Bragg scattering that couples counter-propagating waveguide modes. ^[32]

The two bands observed in **Figure 3.10**, arise from Bragg scattered light into both forward- and backward-propagating TM waveguide modes. The maximum coupling of incident light with the waveguide modes, occurs at angles θ that satisfy equation (3.3),

$$\frac{2\pi}{\lambda} \sin \theta = \pm \frac{2\pi n_{eff}}{\lambda} \pm m \frac{2\pi}{\Lambda} \quad (3.3)$$

where n_{eff} is the effective refractive index of the waveguide, Λ is the grating period, and m is an integer.

In terms of wavevectors, the equation (3.3) can be written as,

$$k_0 \sin \theta = \pm k_{mode} \pm m k_g \quad (3.4)$$

where k_0 is the wavevector of the incident light, k_{mode} is the wavevector of the DFB cavity mode, and k_g is the grating Bragg wavevector.

Equations (3.3) and (3.4) are derived from momentum conservation in the waveguide plane, including integer multiples of the Bragg vector ($k_g = \frac{2\pi}{\Lambda}$) to take into consideration the grating scattering. The \pm signs correspond to light coupling into both counter-propagating waveguide modes. Coupling of light into and out of the waveguide is a result of single k_g scattering ($m = \pm 1$).

The anticrossing behavior at normal incidence arises from the photonic band gap created. The modes that couple to the waveguide from normal incidence have momentum $\pm k_g$, and thus they can couple by $2k_g$ scattering. These counter-propagating modes interfere leading to two standing-wave solutions

at $\theta=0^\circ$. The two standing waves have different energies for the same wavevector, creating a photonic band gap between the two band edges, within which the guided modes cannot propagate because they interfere destructively. ^[33]

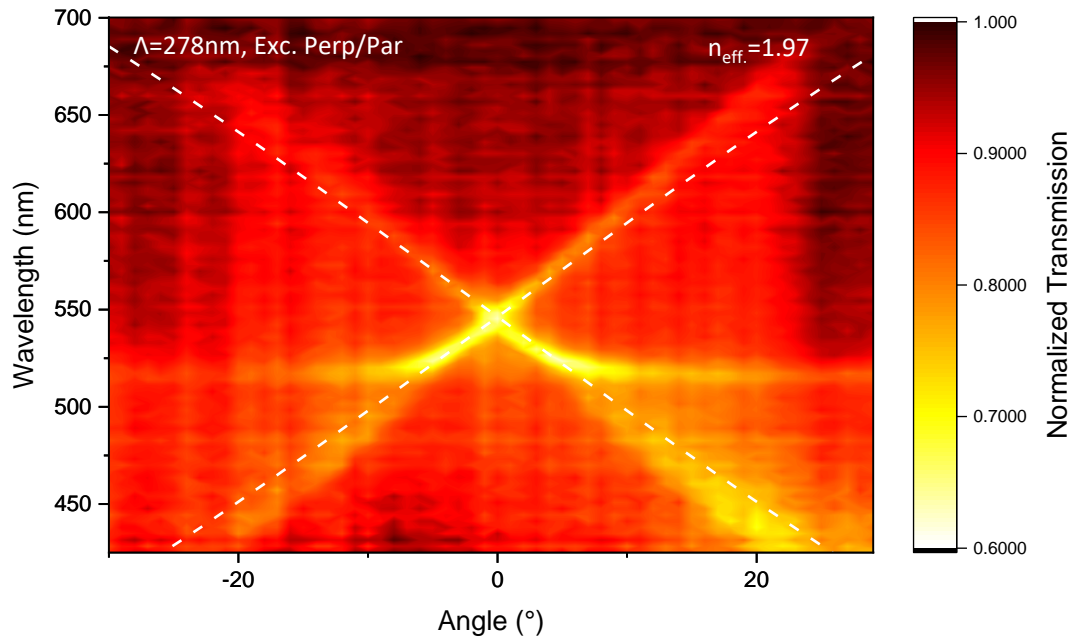


Figure 3.11: Fitting of experimental data of angle-resolved transmission for the $\Lambda=278$ nm structure using the equation (3.3).

Figure 3.11 shows a graph with the fitting of the two bands of the photonic band dispersion for the $\Lambda=278$ nm structure, using the equation (3.3). From the fitting, the effective refractive index of the structure was calculated, and the result is $n_{eff.} = 1.97$.

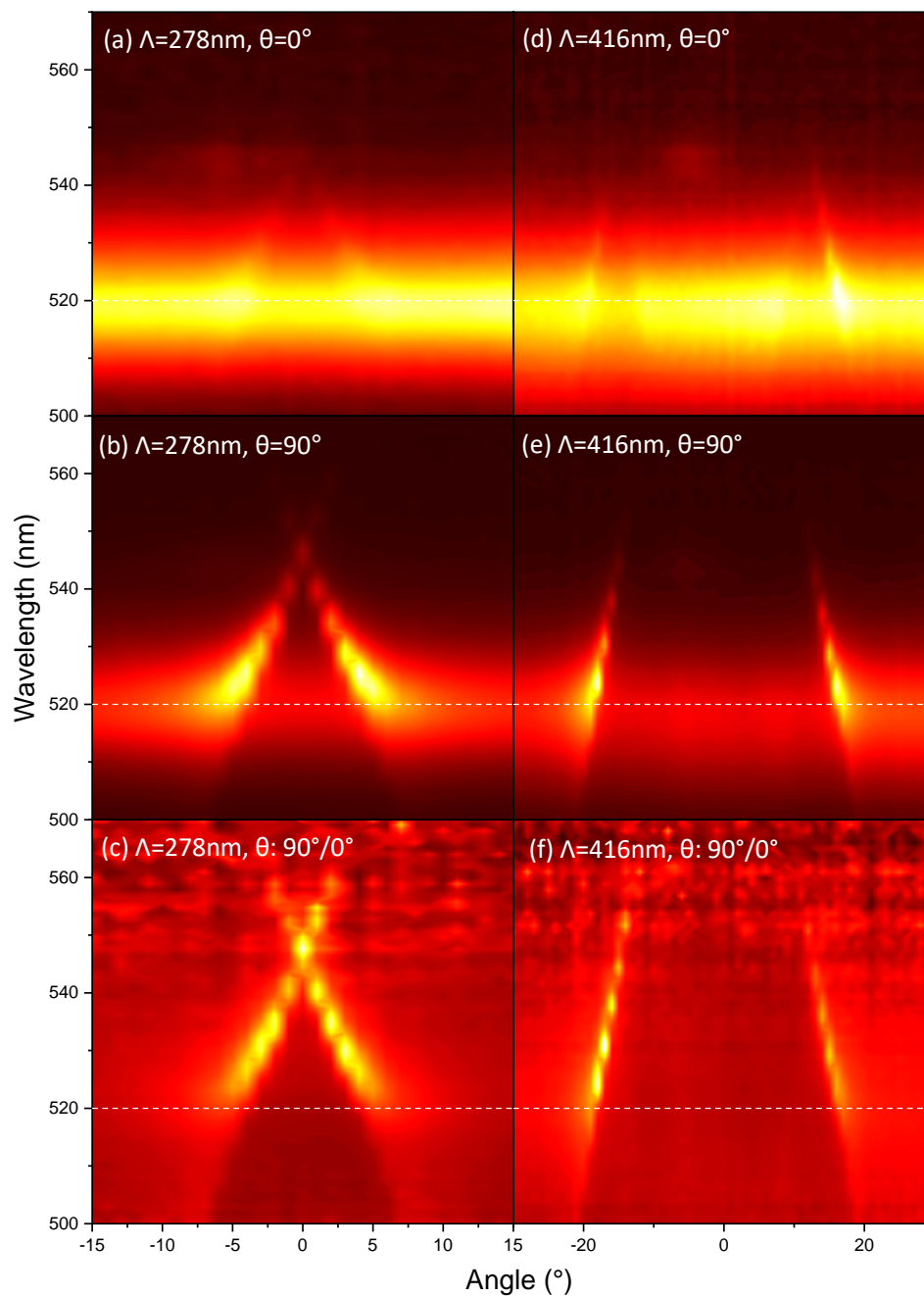


Figure 3.12: Angle-resolved PL spectra of the two DFB gratings under perpendicular excitation. Yellow regions in figure correspond to higher intensity.

In **Figure 3.12**, the measurements for angle-resolved PL of the two DFB gratings under perpendicular excitation are displayed. The emission of the two DFB gratings ($\Lambda=278$ nm and $\Lambda=416$ nm) for polarizer angle $\theta=0^\circ$ (TE mode), is shown in **Figure 3.12 (a)** and **(d)**. The coupling between the emitted light and TE waveguide mode is weak, and thus the observed high PL intensity, centered at $\lambda\sim 520$ nm, is mainly due to NCs emission. **Figure 3.12 (b)** and **(e)** illustrate the emission of the two samples for $\theta=90^\circ$ (TM mode). For the grating with $\Lambda=278$ nm, the graph has two discrete bands that anticross at normal

incidence at $\lambda \sim 546$ nm, in agreement with the transmission measurements (**Figure 3.10 (b)**). The graph for the grating with $\Lambda=416$ nm, has also two discrete bands, however the anticrossing behavior is not visible because it occurs at wavelengths that are not within the emission range of the NCs used. For PL measurements, the two bands correspond to emission peaks of PL coupled into the TM waveguide mode and subsequently Bragg scattered out of the waveguide. In **Figure 3.12 (c)** and **(f)**, the PL measurements for polarizer angle $\theta=90^\circ$ were divided by the PL measurements for $\theta=0^\circ$ to remove the lineshape of NCs emission, enhancing thus the emission of the Bragg scattered light.

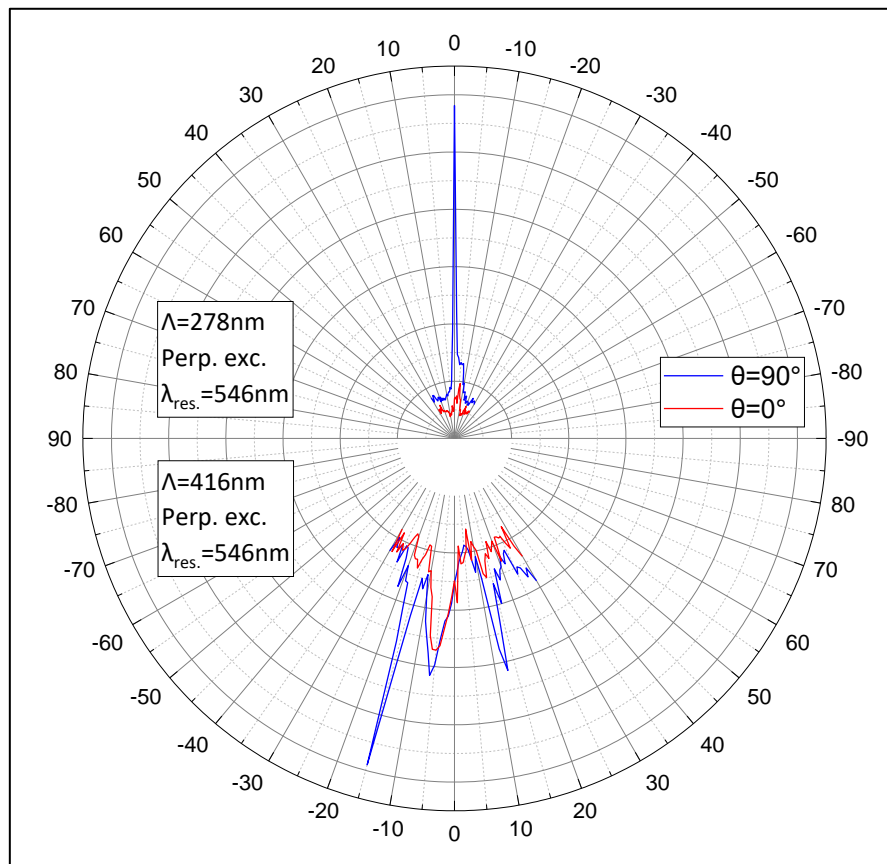


Figure 3.13: Angular distribution of the DFB-NC structure guided mode at $\lambda=546$ nm.

The angular distribution of the guided mode at $\lambda=546$ nm for both samples at angles $\theta=0^\circ$ and $\theta=90^\circ$, is shown in **Figure 3.13**. For the grating with $\Lambda=278$ nm at $\theta=90^\circ$ (TM mode), the mode emission is highly directional with FWHM $\sim 1.5^\circ$.

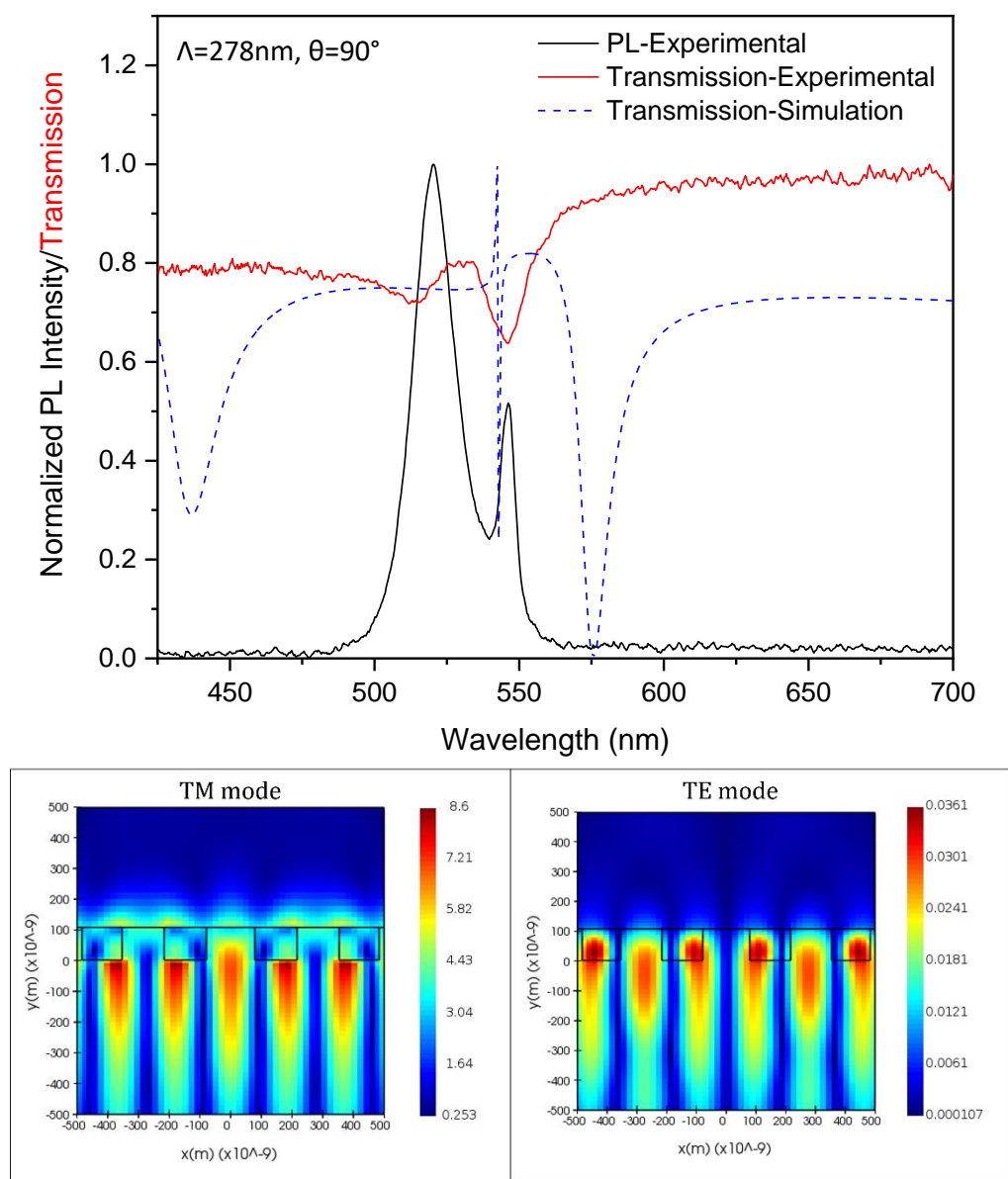


Figure 3.14: Top: PL and transmission spectra at normal incidence of the $\Lambda=278$ nm grating under perpendicular excitation at polarizer angle $\theta=90^\circ$ (TM cavity mode). Also, the transmission spectrum from the FDTD simulations performed is shown in the figure. The parameters used for the simulation are: $\Lambda=278$ nm, height of the grating grooves = 110 nm, fill factor = 0.5, active layer thickness = 110 nm, and refractive indices of the substrate (CdA) and active material ($CsPbBr_3$ NCs), are taken as 1.47 and 2.3, respectively. **Bottom:** TM and TE mode profiles extracted from the FDTD simulations using the same parameters mentioned above.

Figure 3.14 (top) shows the PL and transmission spectra of the $\Lambda=278$ nm DFB grating at normal incidence under perpendicular excitation for polarizer angle $\theta=90^\circ$, and the transmission spectra extracted from the simulations. The experimental transmission spectrum exhibits two local minima, at $\lambda\sim 515$ nm and at $\lambda\sim 546$ nm. The first is assigned to the bandgap of the $CsPbBr_3$ NCs, being consistent with the Stokes shifted emission at $\lambda\sim 520$ nm where the emission of the NCs in the absence

of cavity is peaked. The second at $\lambda \sim 546$ nm is attributed to the TM resonance mode wavelength, as discussed previously in the text. The modeled transmission spectrum exhibits a narrow minimum at $\lambda \sim 543$ nm in the vicinity of the experimentally observed DFB mode, validating the assignment of such a feature. In **Figure 3.14** (bottom) the TM and TE mode profiles obtained from the simulations are illustrated. The mode profiles confirm that the coupling of NC emission with the TM cavity mode is stronger and more efficient as it seems that the light scattered into the TM mode has a higher intensity than the scattered light into the TE mode. In addition, the light for the case of the TM mode, is scattered out of the cavity and the diffraction patterns that are formed are visible.

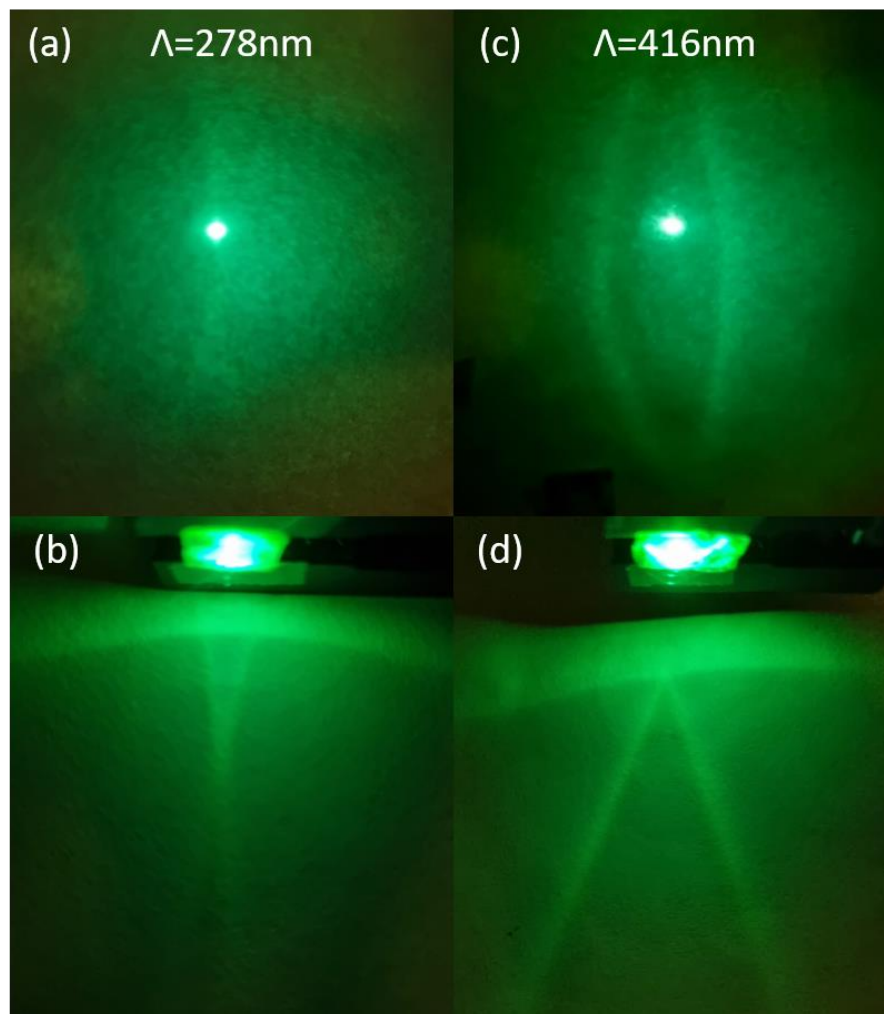


Figure 3.15: Images of the emitted light patterns. Front view **(a)** and top view **(b)** for the grating with $\Lambda = 278$ nm, and front **(c)** and top view **(d)** for the grating with $\Lambda = 416$ nm.

Images in **Figure 3.15**, reveal the far field emission patterns of the two probed DFB gratings. Photos **(a)** and **(b)** show the front and top view, respectively, of the $\Lambda = 278$ nm structure, and photos **(c)** and **(d)** show the front and top view, respectively, of the $\Lambda = 416$ nm structure. In top view images, the anticrossing of the two bands observed in angle-resolved PL and transmission data, is visible.

4. Conclusions and Future Work

Optical studies of nanoimprinted Distributed Feedback Resonators combined with spin coated CsPbBr₃ perovskite nanocrystal overlayers, have been performed. Two types of gratings with period of $\Lambda=278$ nm and $\Lambda=416$ nm have been employed with modifications of the PL intensity, lineshape, and polarization being observed for the former grating.

In the first part of the thesis, the effect of the gratings on the spectral characteristics and the linear polarization of the steady state PL of the DFB-NC structures was investigated. It was found that when the $\Lambda=278$ nm structure was excited with a laser linear polarization perpendicular to the grating grooves, the NC emission was modified via the appearance of a strong resonance peak with high linear polarization up to ~84%. These observations can be interpreted as a result of the coupling between the nanocrystal emission and the TM cavity mode. In contrast, for excitation of the structures with polarization parallel to the grating grooves, no resonance peak in the PL spectrum was observed and the linear polarization of the emission was significantly lower, indicating that the coupling between NC emission and TE cavity mode is weak.

In the second part of this thesis, time-resolved emission (TRPL) from the nanocrystal films deposited on the DFB structures was studied. The TRPL data confirm the steady state measurements, yielding high linear polarization of the emitted light for the structure with period $\Lambda=278$ nm when the resonance peak emission was monitored.

Finally, the photonic band structure of the DFB gratings coated with CsPbBr₃ NCs, was investigated via angle-resolved transmission measurements. The data showed that the incident light is scattered into the TM DFB cavity mode, while the interaction of incident light with TE cavity mode is weak. The obtained photonic band dispersion of the DFB-NC structure further confirms the steady state and time-resolved PL data, with the observed behavior explained by the coupling of NC PL into the TM cavity mode with a subsequent Bragg scattering of the emitted light out of the waveguide.

Future work includes the optimization of the DFB structure and the NC layer to obtain amplified spontaneous emission (ASE) and eventually lasing. In addition, the DFB-NC structures will be combined with blue emitting LEDs to produce polarized sources for display applications.

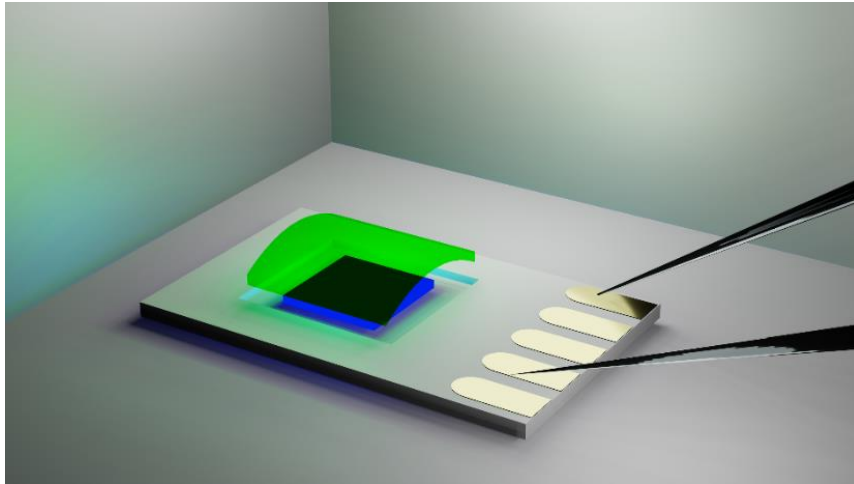


Figure 4.1: Integration of the DFB-NC structure with a blue emitting LED.

5. References

- [1] Gaponenko, S. V. *Optical Properties of Semiconductor Nanocrystals*. (Cambridge University Press, 1998). doi:10.1017/CBO9780511524141.
- [2] Talapin, D. V., Lee, J. S., Kovalenko, M. V. & Shevchenko, E. V. Prospects of colloidal nanocrystals for electronic and optoelectronic applications. *Chem. Rev.* **110**, 389–458 (2010).
- [3] Protesescu, L. *et al.* Nanocrystals of Cesium Lead Halide Perovskites (CsPbX₃, X = Cl, Br, and I): Novel Optoelectronic Materials Showing Bright Emission with Wide Color Gamut. *Nano Lett.* **15**, 3692–3696 (2015).
- [4] Kovalenko, M. V. & Bodnarchuk, M. I. Lead halide perovskite nanocrystals: From discovery to self-assembly and applications. *Chimia (Aarau)*. **71**, 461–470 (2017).
- [5] Murray, C. B., Norris, D. J. & Bawendi, M. G. Synthesis and Characterization of Nearly Monodisperse CdE (E = S, Se, Te) Semiconductor Nanocrystallites. *J. Am. Chem. Soc.* **115**, 8706–8715 (1993).
- [6] De Mello Donegá, C., Liljeroth, P. & Vanmaekelbergh, D. Physicochemical evaluation of the hot-injection method, a synthesis route for monodisperse nanocrystals. *Small* **1**, 1152–1162 (2005).
- [7] Lokhande, A. C., Gurav, K. V., Jo, E., Lokhande, C. D. & Kim, J. H. Chemical synthesis of Cu₂SnS₃ (CTS) nanoparticles: A status review. *J. Alloys Compd.* **656**, 295–310 (2016).
- [8] Kovalenko, M. V., Protesescu, L. & Bodnarchuk, M. I. Properties and potential optoelectronic applications of lead halide perovskite nanocrystals. *Science (80-.)*. **358**, 745–750 (2017).
- [9] Akkerman, Q. A., Rainò, G., Kovalenko, M. V. & Manna, L. Genesis, challenges and opportunities for colloidal lead halide perovskite nanocrystals. *Nat. Mater.* **17**, 394–405 (2018).
- [10] De Roo, J. *et al.* Highly Dynamic Ligand Binding and Light Absorption Coefficient of Cesium Lead Bromide Perovskite Nanocrystals. *ACS Nano* **10**, 2071–2081 (2016).
- [11] Bodnarchuk, M. I. *et al.* Rationalizing and Controlling the Surface Structure and Electronic Passivation of Cesium Lead Halide Nanocrystals. *ACS Energy Lett.* **4**, 63–74 (2019).
- [12] Kavokin, A., Baumberg, J. J., Malpuech, G. & Laussy, F. P. *Microcavities*. (Oxford University Press, 2007). doi:10.1093/acprof:oso/9780199228942.001.0001.
- [13] Yakunin, S. *et al.* Low-threshold amplified spontaneous emission and lasing from colloidal nanocrystals of caesium lead halide perovskites. *Nat. Commun.* **6**, (2015).
- [14] Fu, Y. & Zhai, T. Distributed feedback organic lasing in photonic crystals. *Front. Optoelectron.* **13**, 18–34 (2020).

- [15] Samuel, I. D. W. & Turnbull, G. A. Organic semiconductor lasers. *Chem. Rev.* **107**, 1272–1295 (2007).
- [16] Lova, P., Manfredi, G. & Comoretto, D. Advances in Functional Solution Processed Planar 1D Photonic Crystals. *Adv. Opt. Mater.* **6**, (2018).
- [17] De Giorgi, M. L. & Anni, M. Amplified spontaneous emission and lasing in lead halide perovskites: State of the art and perspectives. *Appl. Sci.* **9**, (2019).
- [18] Smirnov, J. R. C. *et al.* Flexible distributed feedback lasers based on nanoimprinted cellulose diacetate with efficient multiple wavelength lasing. *npj Flex. Electron.* **3**, 1–7 (2019).
- [19] Pourdavoud, N. *et al.* Room-Temperature Stimulated Emission and Lasing in Recrystallized Cesium Lead Bromide Perovskite Thin Films. *Adv. Mater.* **31**, (2019).
- [20] Liew, S. C. Computer Modelling and Analysis of Multisection DFB Lasers. *Thesis* (1995).
- [21] Kogelnik, H. & Shank, C. V. Coupled-wave theory of distributed feedback lasers. *J. Appl. Phys.* **43**, 2327–2335 (1972).
- [22] Bonal, V., Quintana, J. A., Villalvilla, J. M., Boj, P. G. & Díaz-García, M. A. Controlling the emission properties of solution-processed organic distributed feedback lasers through resonator design. *Sci. Rep.* **9**, 11159 (2019).
- [23] Zhang, J. X. J. & Hoshino, K. *Fundamentals of nano/microfabrication and scale effect. Molecular Sensors and Nanodevices* (2019). doi:10.1016/b978-0-12-814862-4.00002-8.
- [24] Mishra, A., Bhatt, N. & Bajpai, A. K. *Nanostructured superhydrophobic coatings for solar panel applications. Nanomaterials-Based Coatings: Fundamentals and Applications* (Elsevier Inc., 2019). doi:10.1016/B978-0-12-815884-5.00012-0.
- [25] Sahu, N., Parija, B. & Panigrahi, S. Fundamental understanding and modeling of spin coating process: A review. *Indian J. Phys.* **83**, 493–502 (2009).
- [26] Abu-kmail, M. Y. Activity Behavior of Human Serum Albumin Doped in Silica Sol-Gel Thin Film.
- [27] PerkinElmer. LAMBDA UV/Vis and UV/Vis/NIR Spectrophotometers. (2012).
- [28] HORIBA. A practical guide to time-resolved luminescence lifetime determination using dedicated Time-Correlated Single-Photon Counting systems. 1–31.
- [29] Becker, W. *Introduction to Multi-dimensional TCSPC.* (2015). doi:10.1007/978-3-319-14929-5.
- [30] OceanOptics. Usb2000+. (2005).
- [31] Lichtman, J. W. & Conchello, J. A. Fluorescence microscopy. *Nat. Methods* **2**, 910–919 (2005).
- [32] Jory, M. J., Barnes, W. L., Samuel, I. D. W., Turnbull, G. A. & Andrew, P. Relationship between photonic band structure and emission characteristics of a polymer distributed feedback laser.

- Phys. Rev. B - Condens. Matter Mater. Phys.* **64**, 1–6 (2001).
- [33] Andrew, P., Turnbull, G. A., Samuel, I. D. W. & Barnes, W. L. Photonic band structure and emission characteristics of a metal-backed polymeric distributed feedback laser. *Appl. Phys. Lett.* **81**, 954–956 (2002).
- [34] Csele M. Fundamentals of light sources and lasers. (2004)
- [35] Lumerical Inc. Finite Difference Time Domain (FDTD) solver introduction. [Online] <https://support.lumerical.com/hc/en-us/articles/360034914633-FDTD-solver>
- [36] Fox M. Optical Properties of Solids. *Oxford University Press*. (2001)

Appendix

Optical modelling

1. Variation of grating period

Firstly, the impact of the variation of grating period on the intensity, linewidth and wavelength of the resonances was investigated. The fixed parameters were: (i) the height of the grating grooves, $h=110$ nm, (ii) the active layer thickness= 110 nm, (iii) the fill factor, $F=0.5$, and (iv) the refractive indices of the substrate and active material, 1.47 and 2.3 , respectively.

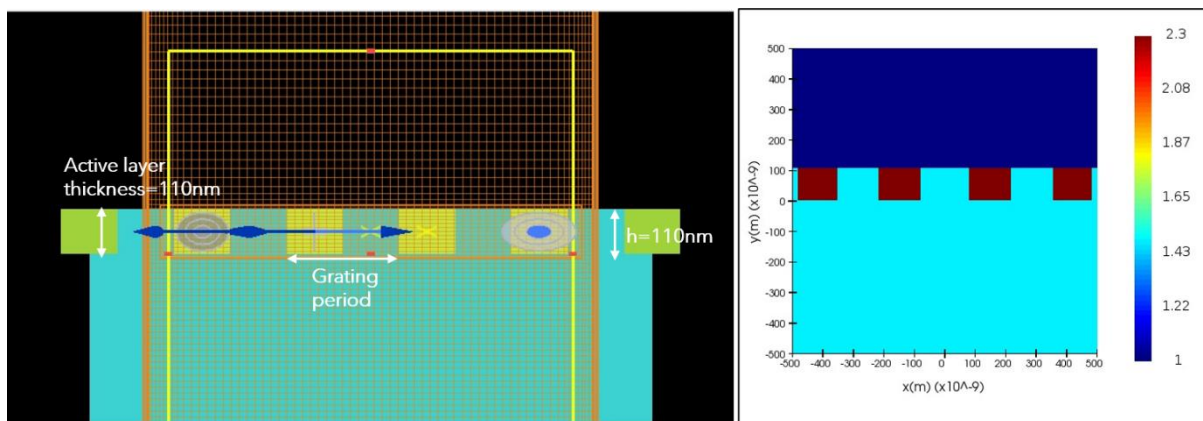


Figure A. 1: **Left:** Illustration of the simulation for the DFB grating with $CsPbBr_3$ NCs as the active material. **Right:** Refractive index map. The light blue corresponds to the substrate (cellulose diacetate CdA) with refractive index 1.47 , and the dark red to the NCs with refractive index 2.3 .

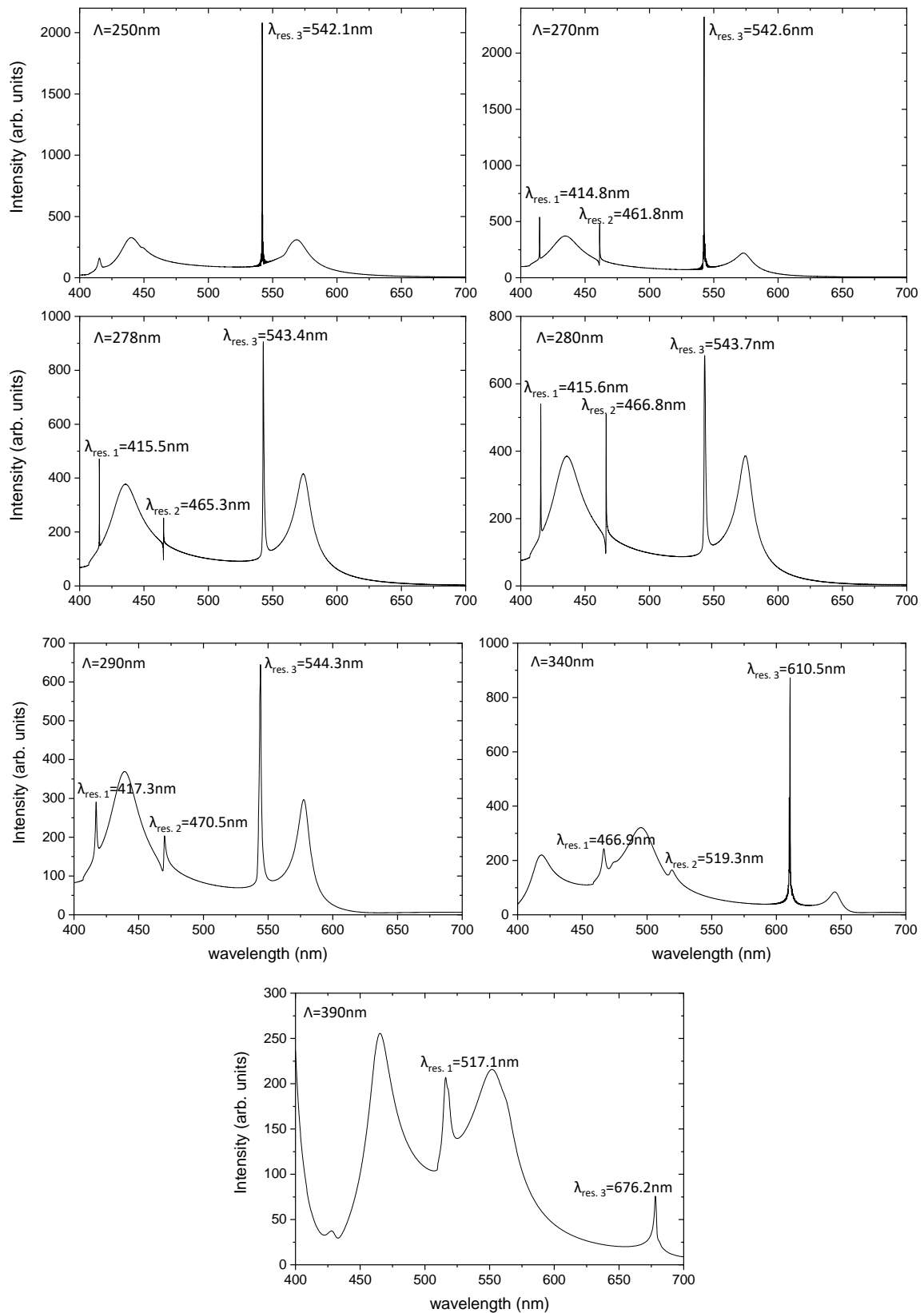


Figure A. 2: Emission spectra for each grating period investigated. The three main resonances of the cavity are shown in the graphs, and the variation of their intensity, linewidth and wavelength can be seen.

In **Figure A. 2** the emission spectra for the investigated grating periods are illustrated. In the graphs, three main resonances are seen. Overall, the resonances seem to move to larger wavelengths with increasing grating period and their linewidth increases. These observations can be confirmed from the graphs in **Figure A. 3**. **Figure A. 3 (a)** illustrates the resonance wavelength over the grating period. It is clear that all the resonances move to larger wavelengths (red shift) with increasing grating period, in agreement with the Bragg's law, $m\lambda = 2n_{eff}\Lambda$. Furthermore, an increase of the resonance linewidth can be observed in **Figure A. 3 (b)**. The Q-factor of the DFB resonator was calculated via the relation,

$$Q\text{-factor} = \frac{\lambda}{\Delta\lambda} \quad (1)$$

where λ is the resonance peak wavelength, and $\Delta\lambda$ is the linewidth (FWHM) of each resonance. **Figure A. 3 (c)** displays the Q-factor of the three resonances over the grating period. In general, Q-factor decreases with increasing grating period for all the resonances. There is an increase of the Q-factor for $\Lambda=340$ nm for the resonance 3.

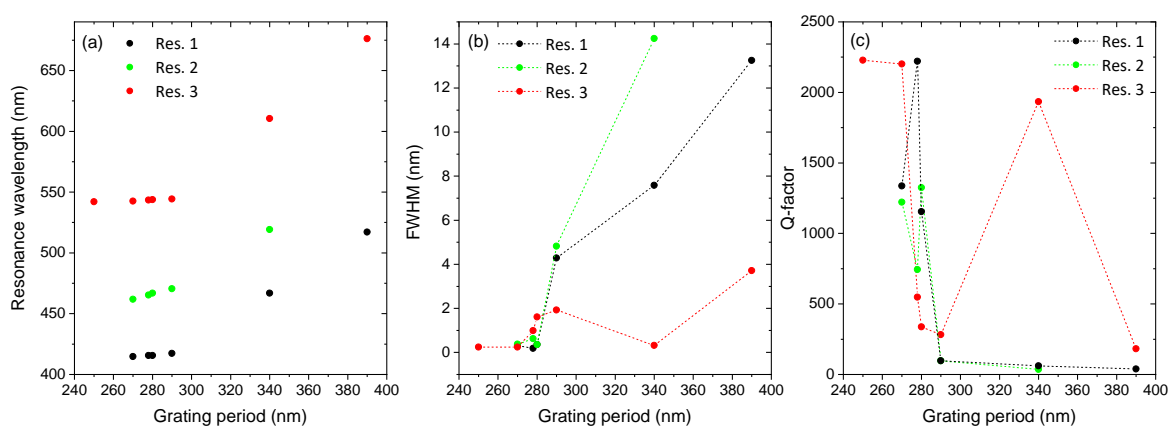


Figure A. 3: (a) Resonance wavelength of the three main resonances shown in Figure A. 2, over the grating period. (b) FWHM of the three resonances over the grating period. The resonance wavelength and the FWHM were calculated via integration of the resonances in emission spectra. (c) Q-factor of the three resonances over the grating period.

From the three main resonances observed, resonance 3 is the resonance of interest because its wavelength is within the emission range of the NCs used. According to Bragg's law, this resonance can be assigned to second order diffraction.

The transmission spectra for the different grating periods, are shown in **Figure A. 4 (a)**. A red shift of the resonance 3 is observed in the graph. The red shift of the resonance 3, is also pronounced in reflectivity spectra in **Figure A. 4 (b)**. These results, further confirm the results emerging from emission spectra, discussed above. **Figure A. 4 (c)** shows the emission and transmission spectra for grating

period $\Lambda=278$ nm. There is an evident accordance between the two spectra, with a narrow resonance observed at $\lambda\sim 543$ nm in both spectra.

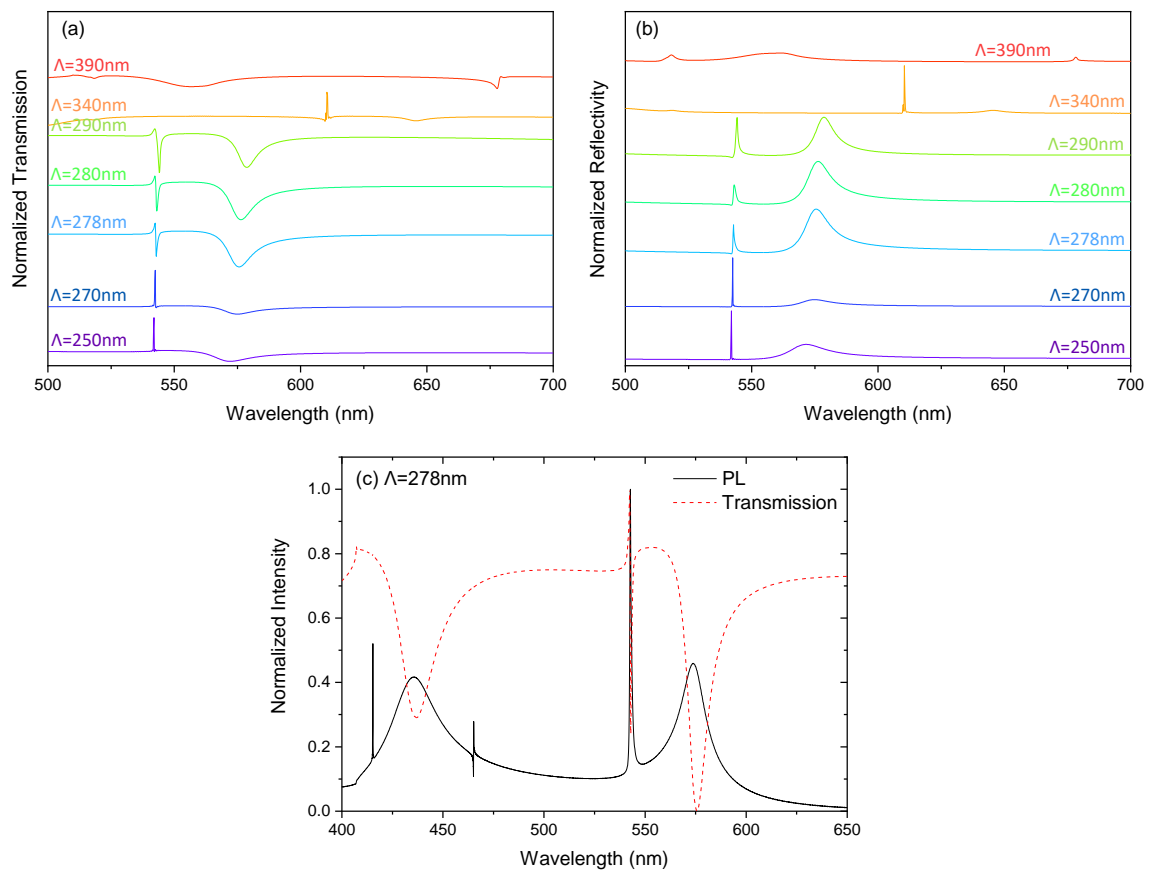


Figure A. 4: (a) Transmission spectra for the investigated grating periods. In the spectra the resonance wavelength variation can be seen. (b) Reflectivity spectra for the different grating periods. (c) Emission and transmission spectra for grating period $\Lambda=278$ nm. A narrow resonance at $\lambda=543$ nm is observed in both spectra.

The electric and magnetic field profiles of the three resonances are illustrated in **Figure A. 5**.

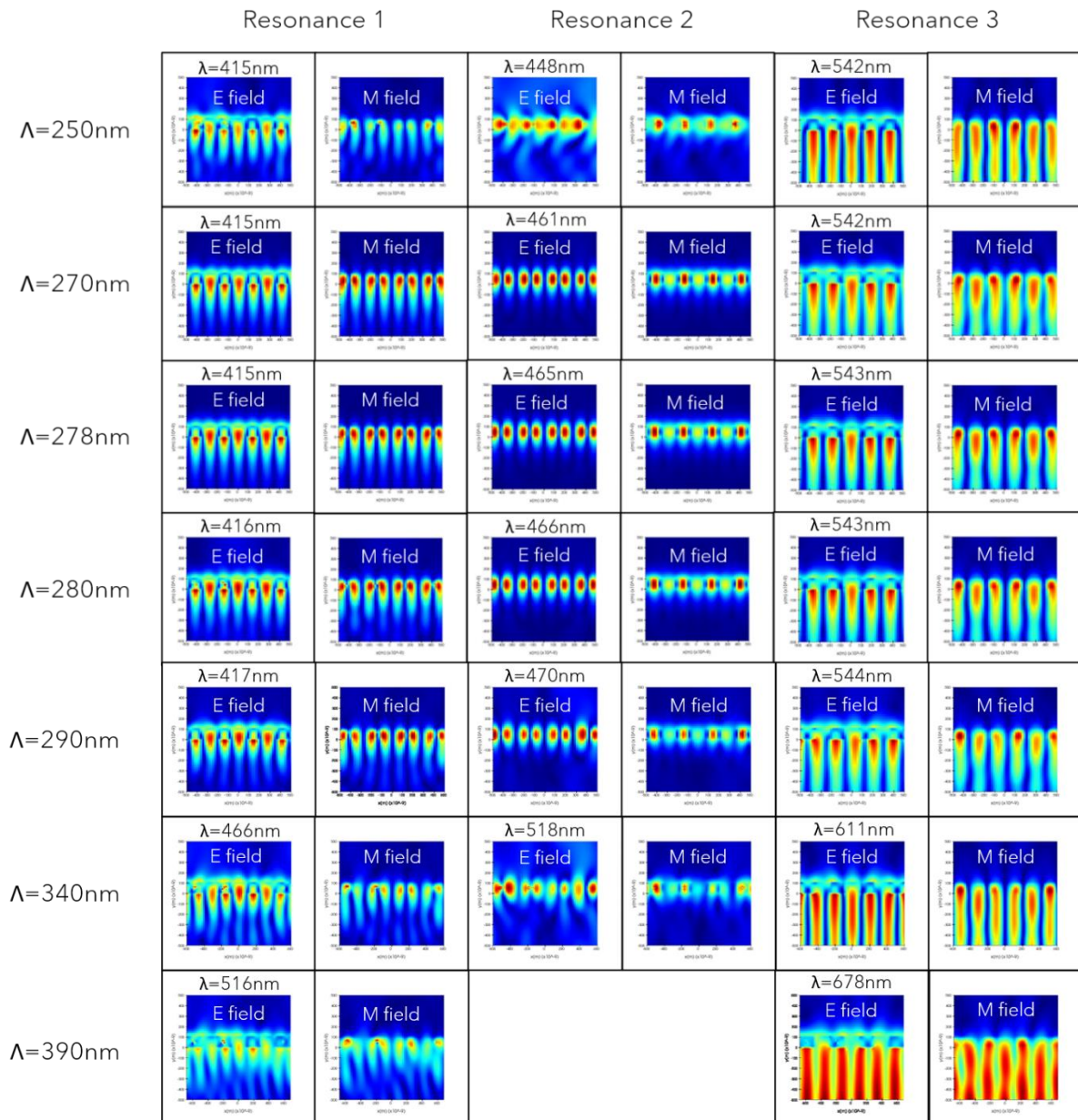


Figure A. 5: Electric and magnetic field profiles of the resonances.

2. Variation of height of grating grooves

In this part, the height of the grating grooves was varied, in order to probe the impact of this variation on wavelength, intensity, and linewidth of the resonances. The fixed parameters were: (i) the grating period, $\Lambda=278$ nm, (ii) the active layer thickness=110 nm, (iii) the fill factor, $F=0.5$, and (iv) the refractive indices of the substrate and active material, 1.47 and 2.3, respectively.

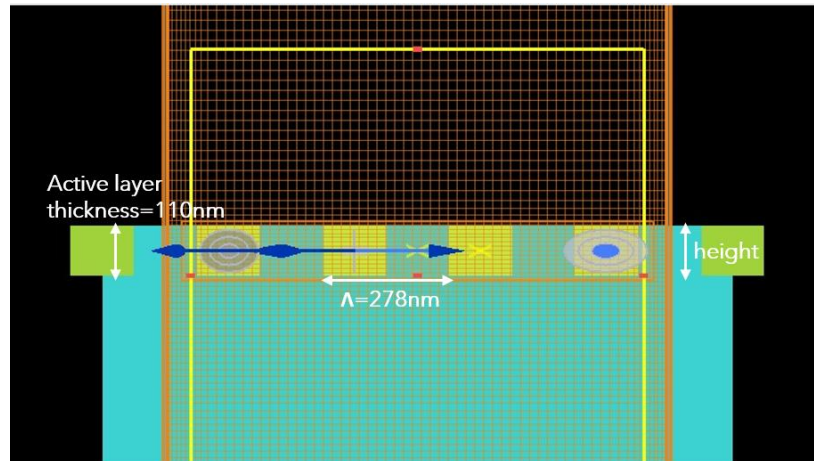


Figure A. 6: Illustration of the simulation of DFB grating.

Figure A. 7 displays the emission spectra for different heights of the grating grooves. From the graphs in figure, a red shift of the resonances wavelengths can be seen. The red shift of the resonance wavelength with increasing height of the grating grooves, is also evident in **Figure A. 8 (a)**. The linewidth of the resonances (**Figure A. 8 (b)**) is higher for heights under 100 nm, and it becomes minimum (< 1 nm) at $h=100$ nm for resonances 1 and 3. For resonance 2, the linewidth is minimum at $h=150$ nm. The Q-factor behavior is shown in **Figure A. 8 (c)**. The Q-factor value is maximum at $h=110$ nm for the resonances 1 and 3, and at $h= 150$ nm for the resonance 2.

In **Figure A. 9**, transmission and reflectivity spectra for the heights of grating grooves under investigation, are displayed. The two graphs show again the red shift of resonance 3, confirming the results arise from emission spectra.

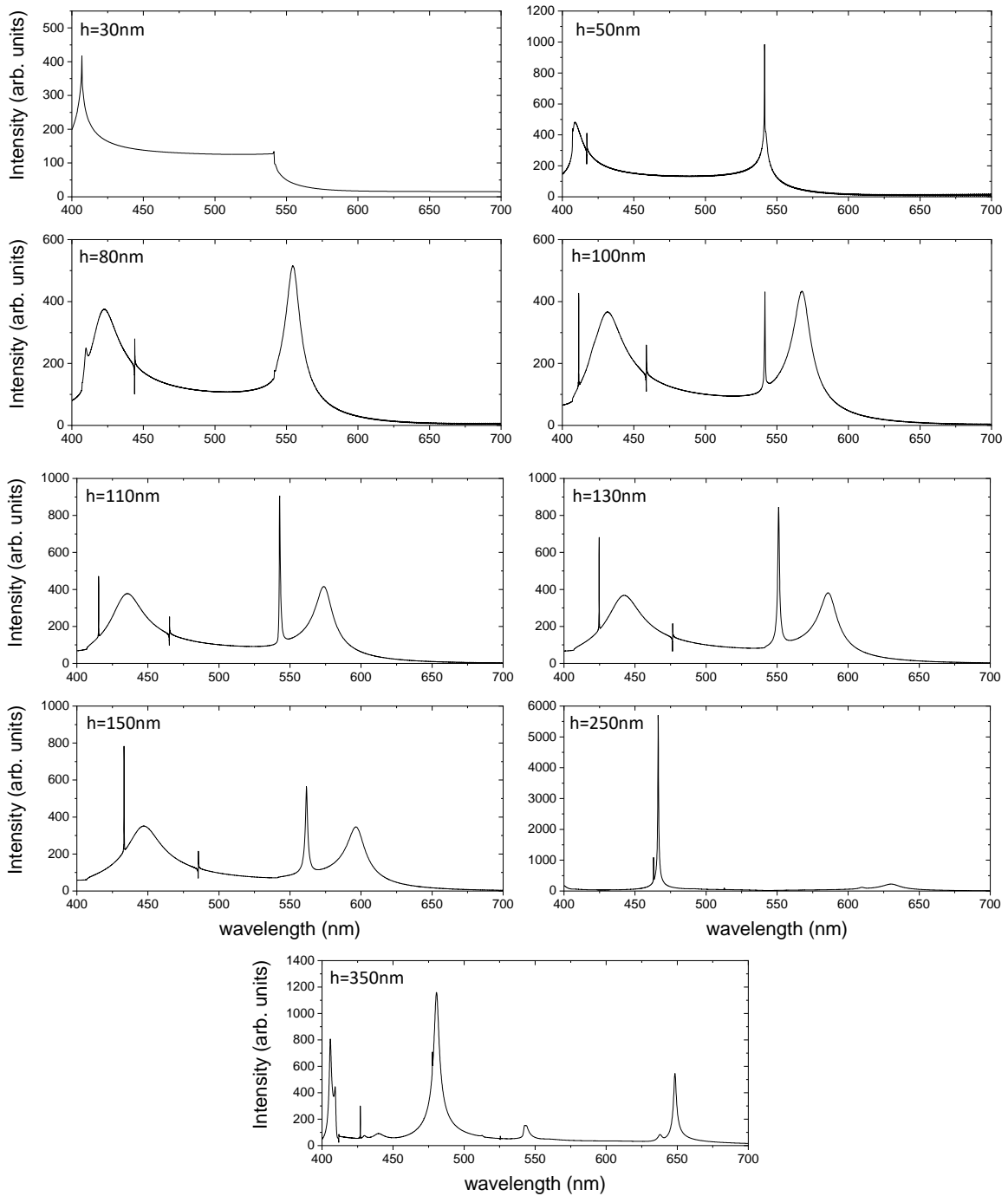


Figure A. 7: Emission spectra for the investigated heights of the grating grooves.

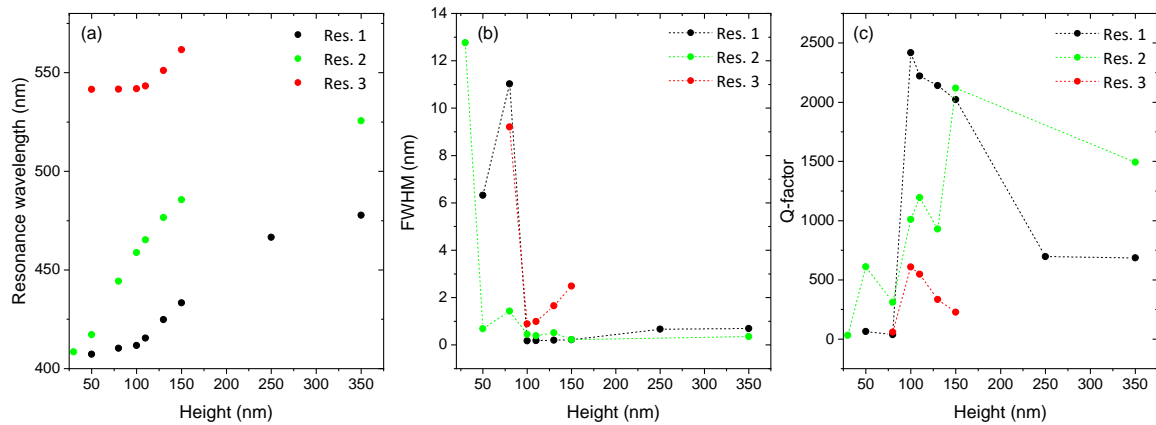


Figure A. 8: (a) Resonance wavelength of the three main resonances observed in Figure A. 7, over the height of the grating grooves. (b) FWHM of the three resonances over the height. The resonance wavelength and the FWHM were calculated via integration of the resonances in emission spectra. (c) Q-factor of the three resonances over the height.

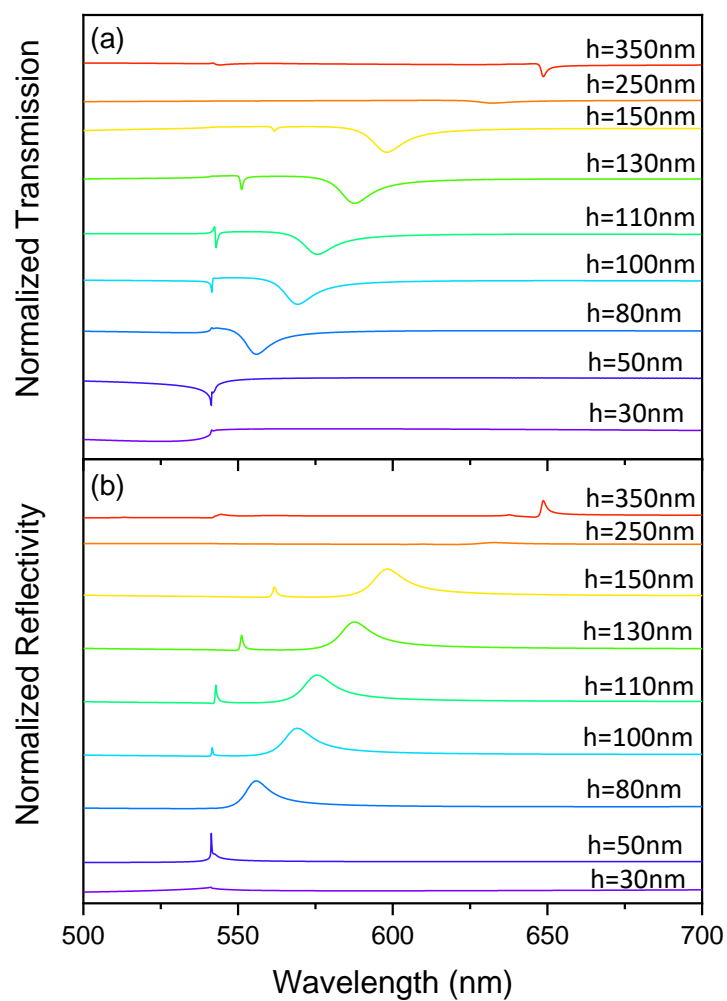


Figure A. 9: Transmission (a) and reflectivity (b) spectra for the different heights of the grating grooves.

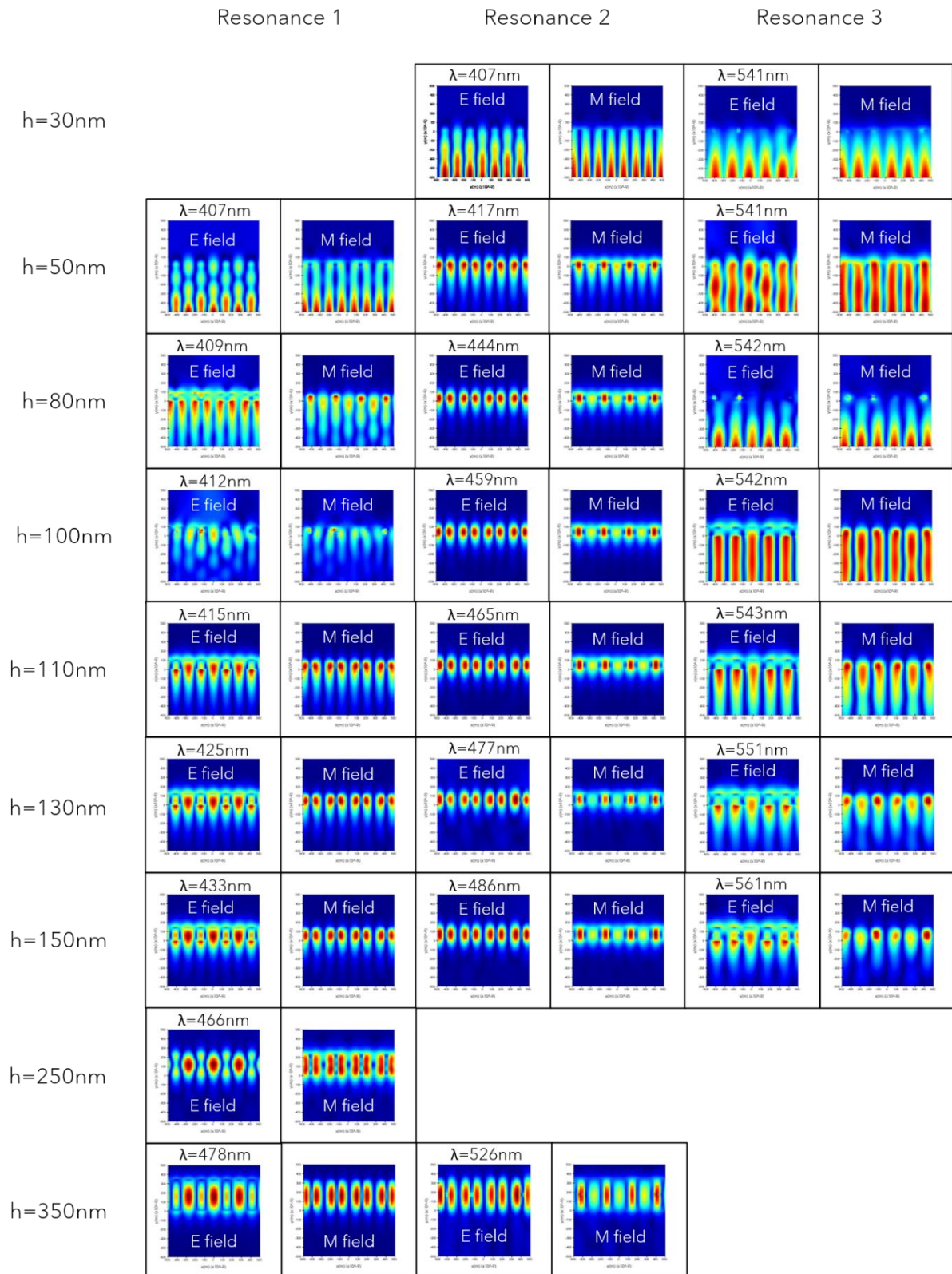


Figure A. 10: Electric and magnetic field profiles of the resonances for the investigated heights of the grating grooves.

3. Variation of active layer thickness

The last parameter investigated, is the active layer thickness. Active layer thickness was varied to probe the impact of its variation on wavelength, intensity, and linewidth of the resonances. The fixed parameters were: (i) the grating period, $\Lambda=278$ nm, (ii) the height of the grating grooves=110 nm, (iii) the fill factor, $F=0.5$, and (iv) the refractive indices of the substrate and active material, 1.47 and 2.3, respectively.

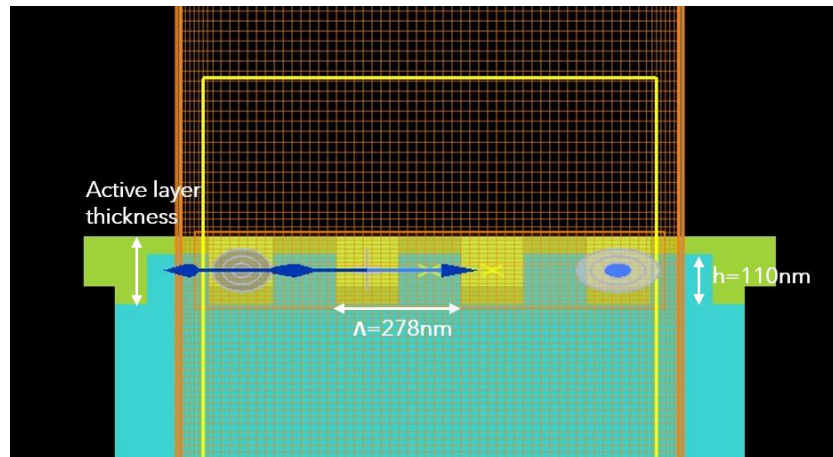


Figure A. 11: Illustration of the simulation of DFB grating. In this case active layer thickness was the parameter under investigation.

The emission spectra for the investigated active layer thicknesses, are seen in **Figure A. 12**. In the graphs, three main resonances are evident again, and a red shift of the peak wavelength is observed. The red shift of the resonance wavelength with increasing active layer thickness is shown clearly in **Figure A. 13 (a)**. The linewidth of the resonances 1 and 2 is approximately unchanged over the active layer thickness, with values < 1 nm. In contrast, the linewidth for resonance 3 increases for a ≥ 170 nm (**Figure A. 13 (b)**). The behavior of the Q-factor of DFB resonator modes can be seen in **Figure A. 13 (c)**. For the resonances 1 and 2, the Q-factor does not show significant variation, while a reduction of the Q-factor is observed for the resonance 3.

Figure A. 14 illustrates the transmission and reflectivity spectra for the probed active layer thicknesses. In both graphs is obvious that the increase of active layer thickness results in a red shift of the resonance peak wavelength (resonance 3), as it was derived from the emission spectra as well.

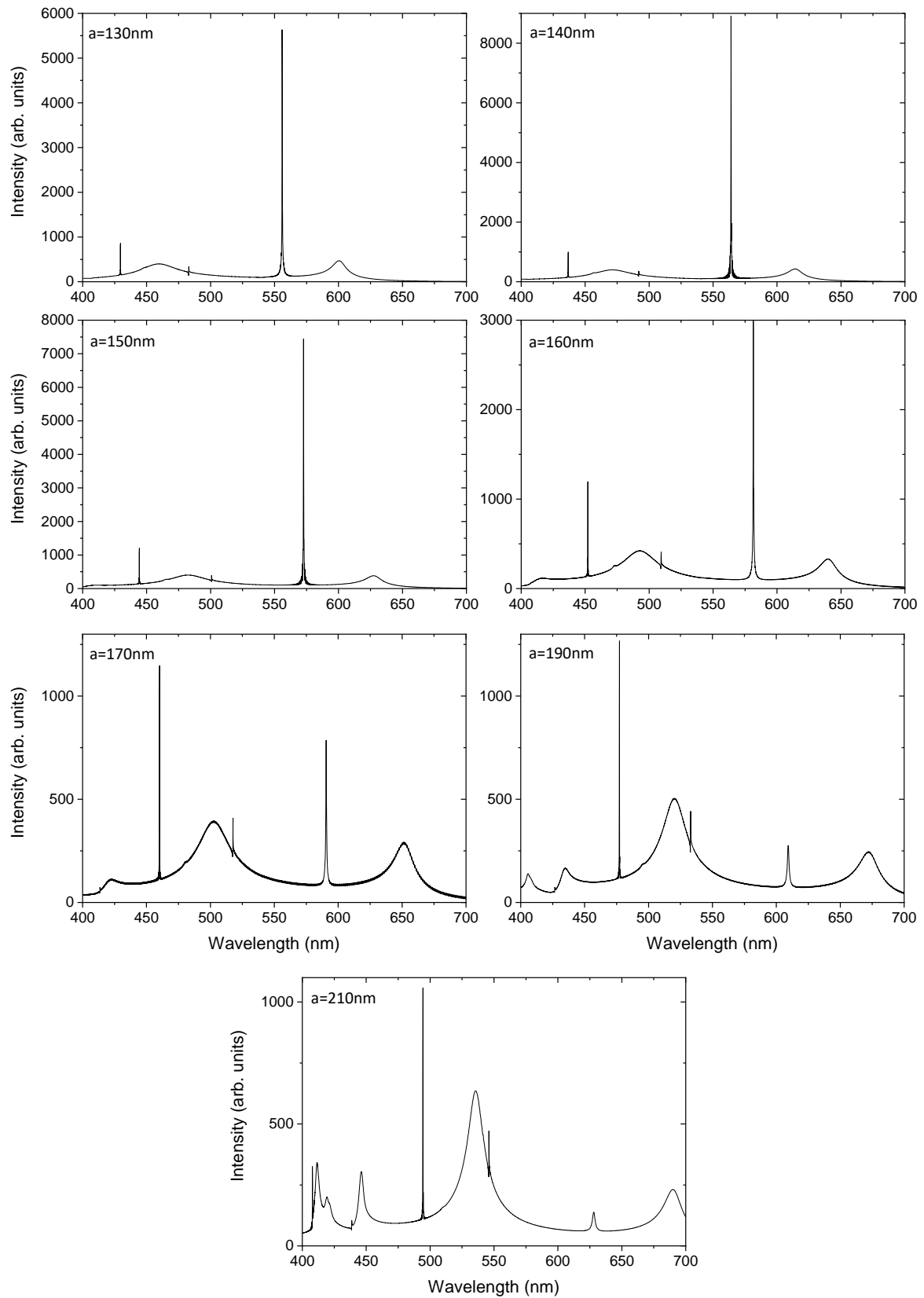


Figure A. 12: Emission spectra for the active layer thicknesses, a , under investigation.

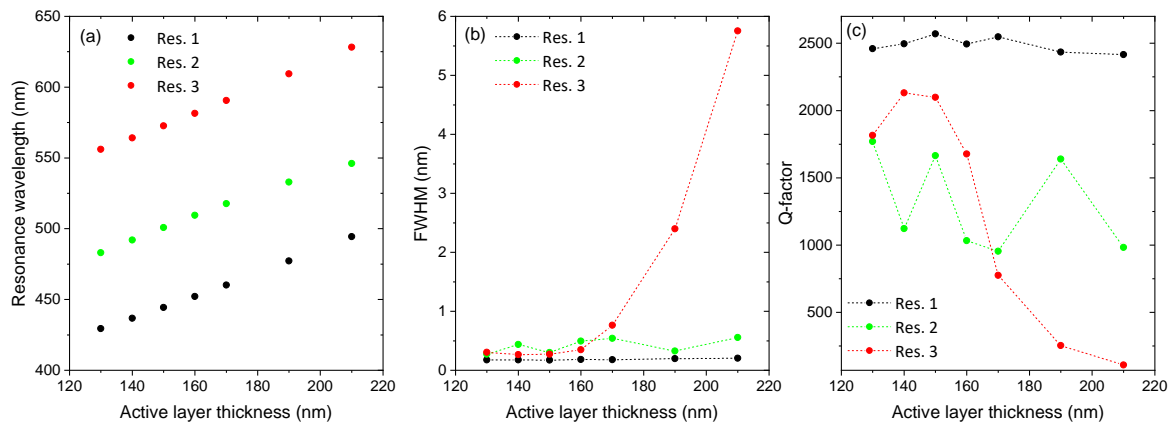


Figure A. 13: (a) Resonance wavelength of the three main resonances observed in Figure A. 12, over the active layer thickness. FWHM (b) and Q-factor (c) of the three resonances over the active layer thickness.

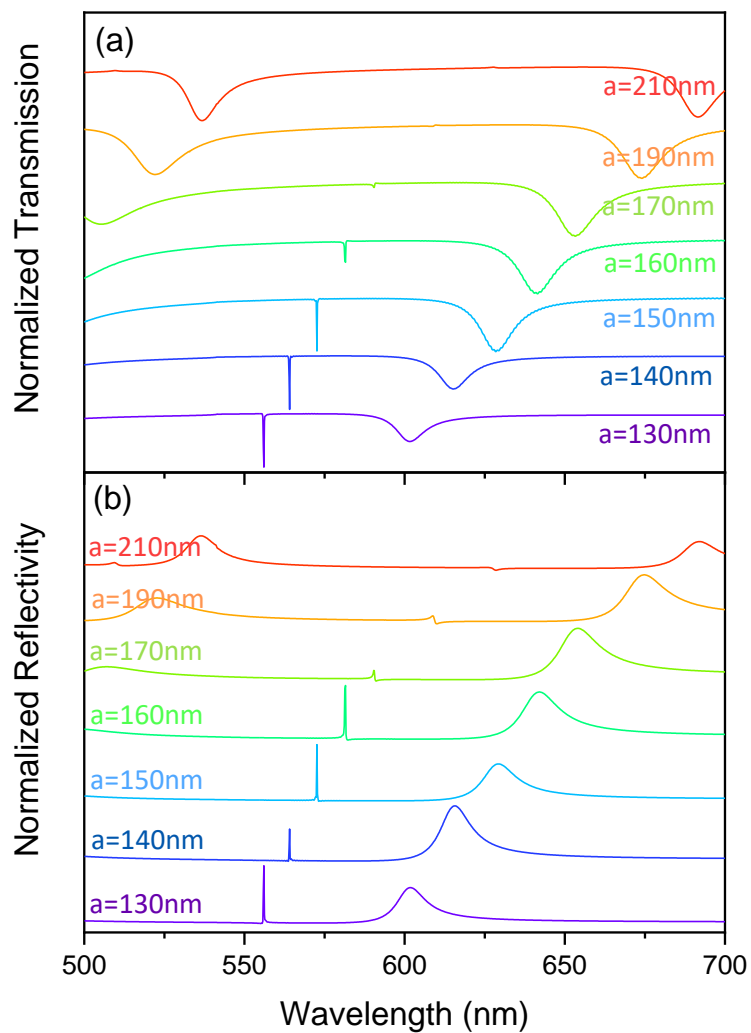


Figure A. 14: Transmission (a) and reflectivity (b) spectra for the investigated active layer thicknesses.

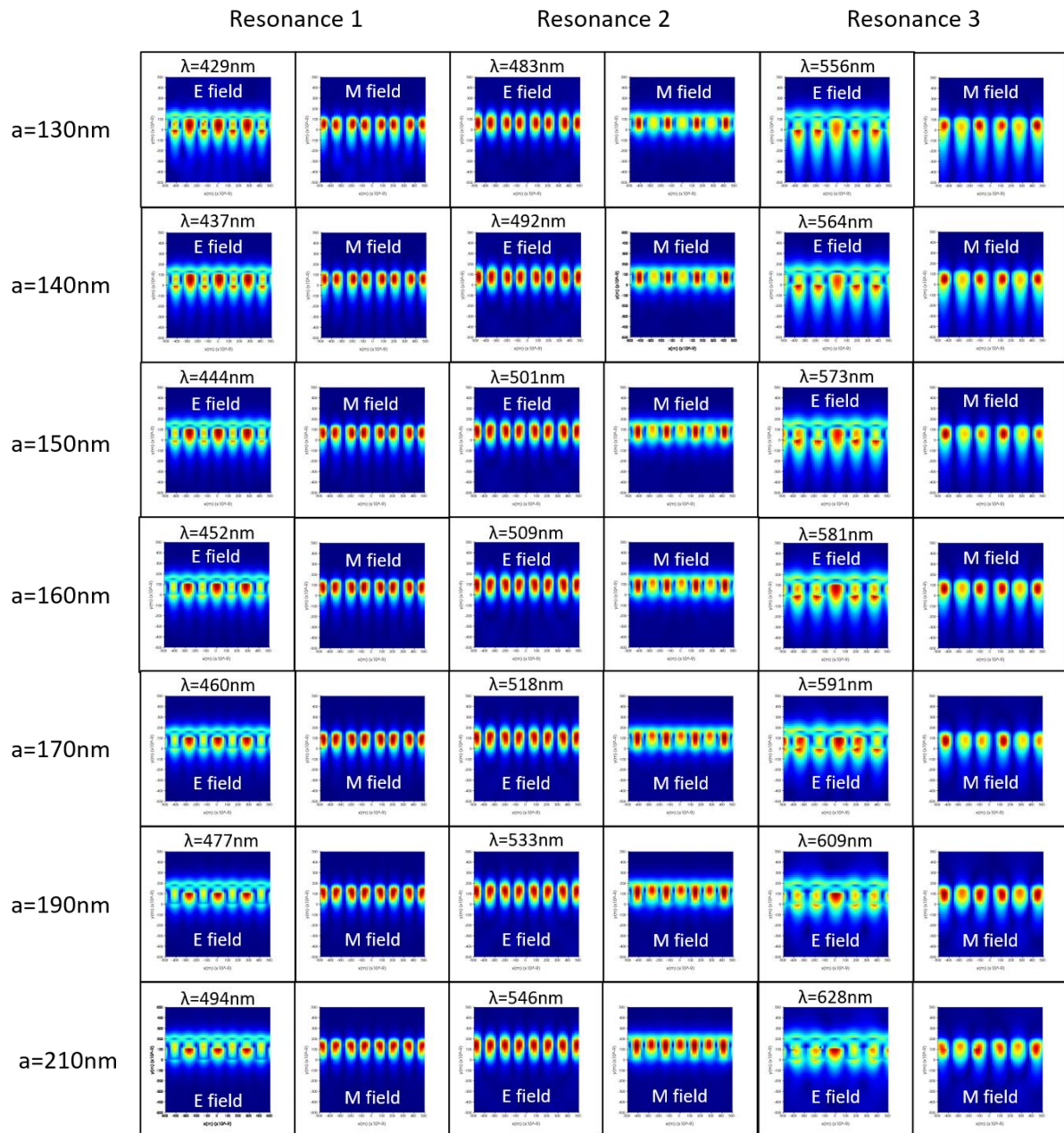


Figure A. 15: Electric and magnetic field profiles of the resonances for the different layer thicknesses.